AMAS COURSE ON MECHANICS OF ADVANCED MATERIALS
MAM'2001 - (PP.369-445) - WARSAW, OCTOBER 8-12, 2001.

Mechanics of bulk ceramics

J. RÖDEL

Institute of Materials Science
University of Technology
D-64287 Darmstadt, Germany

I. Toughening mechanisms in ceramics

1. Theory of R-curves

In contrast to metals, ceramics are not able to dissipate energy in front of the crack tip by a plastic zone. In order to increase the fracture toughness mechanisms have to work at the crack wake. In other words, the goal is to delocalize the damage.

Below the mathematical concept will be introduced:

Stress intensity factor K	Point of view	Energy release rate G	
no R-curve:			
$K_A = K_0$		$G = R$	(1.1)
R-curve:			
$K_A - K_\mu = K_0$	Physician	$G_A - R_\mu = R_0$	(1.2)
$K_A = K_\mu + K_0 = K_R(c)$	Engineer	$G_A = R_0 + R_\mu = R(c)$	(1.3)

where:

- K_A - applied stress intensity factor,
- K_0 - crack tip toughness,
- K_μ - shielding term,
- $K_R(c)$ - fracture toughness as a function of crack length,
- $R(c)$ - crack resistance as a function of crack length,
- G_A - total energy release rate,

with K_0 and K_μ calculated by integration in the crack plane over the length of the cohesive zone λ, or alternatively over the length of the bridging zone c_b.

R_0 and R_μ can be calculated by an integration of the crack closure stresses over the crack opening until the maximum opening of the cohesive zone u^*, or alternatively until the maximum opening of the bridging zone u_b.

Stress intensity factor K	Energy release rate G	
$K_0 = \sqrt{\frac{2}{\pi}} \int_0^{\lambda} g(c,r)\, p_1(r)\, dr$	$R_0 = 2 \int_0^{u^*} p_1(u)\, du$	(1.4)
$K_\mu = \sqrt{\frac{2}{\pi}} \int_0^{c_b} g(c,r)\, p_2(r)\, dr$	$R_\mu = 2 \int_0^{u_b} p_2(u)\, du$	(1.5)

where:

$p_{1,2}$ – closure stress,
$g(c,r)$ – weight function.

The closure stress-crack opening functions $p(u)$ give a unique description of the crack shielding. The R-curves as a function of grain size ($R(c)$ and $K_R(c)$) are in closer detail functions of the exact crack length and of the crack/sample geometry.

Due to the closure stresses p the crack tip is partially shielded from the applied stresses. This causes the crack opening profile to be more compressed than that of a material without shielding. Also, the stress field in front of the crack tip doesn't increase as much as in materials without R-curve behaviour.

K and G can be converted into one another starting from:

$$K_0^2 = G_0\, E', \tag{1.6}$$

$$K_A^2 = G_A\, E', \tag{1.7}$$

one receives:

$$K_\mu = \sqrt{K_0^2 + R_\mu\, E'} - K_0. \tag{1.8}$$

in the case of

- strong shielding: $R_\mu \gg R_0$

$$K_\mu = \sqrt{E'\, R_\mu}, \tag{1.9}$$

- weak shielding: $R_\mu \ll R_0$

$$K_\mu = \frac{R_\mu\, E'}{2K_0}, \tag{1.10}$$

where:

E' – Young's modulus,
G_0 – energy release rate acting at the crack tip.

Depending on the rise of the R-curve and the length of the crack the influence on the fracture strength of the material varies. For short cracks and flat R-curves the tangent point will not change. For long cracks (flat K_a(c)) and steep R-curves the fracture strength of the material can be increased substantially (Fig. 1).

The Griffith-equation has to be modified:

$$\sigma_f = \frac{\sqrt{\pi}}{2} \frac{K_R(c_i)}{\sqrt{c_i}}. \tag{1.11}$$

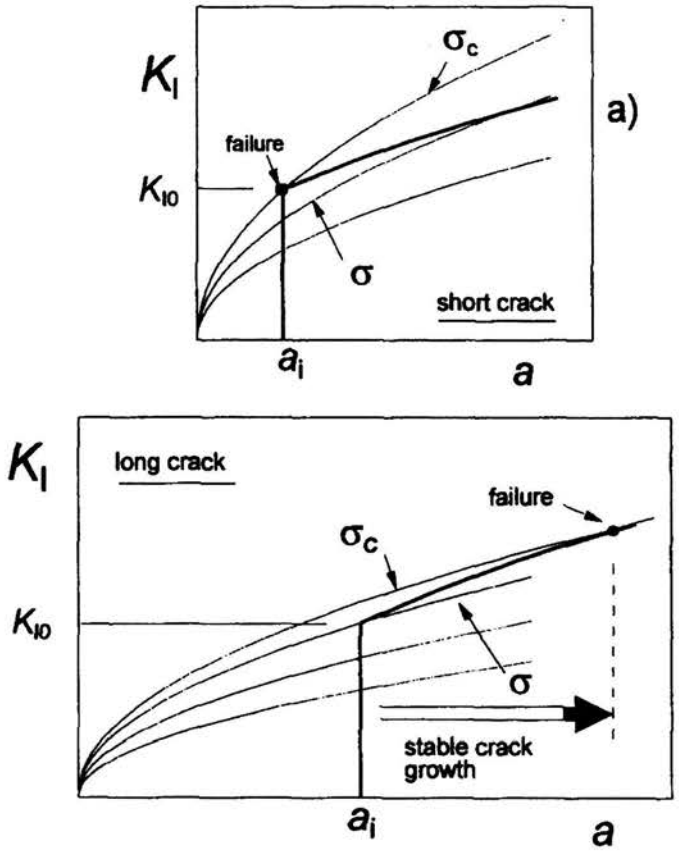

FIGURE 1. Impact of crack length and slope of the R-curve on the fracture strength [1].

The fracture toughness for the initial crack length has been replaced by the fracture toughness at the point of instability ($K_R(c_i)$). The respective crack length is c_i.

Since the effect is larger for long cracks there is also a positive effect on the variability of the fracture strength. For constant defect population and for a steep R-curve the scatter of the fracture strength will be decreased.

2. Crack bridging

2.1. General considerations

A classification of crack bridging can be done by material classes (e.g. fibre-reinforced materials) or by the kind of mechanism that leads to an increase in the strength of the material. The following distinction can be made by the second option (Fig. 2):

(a) elastic bridge,
(b) frictional bridge,
(c) combination of (a) and (b), also called interlocking,
(d) ductile bridge.

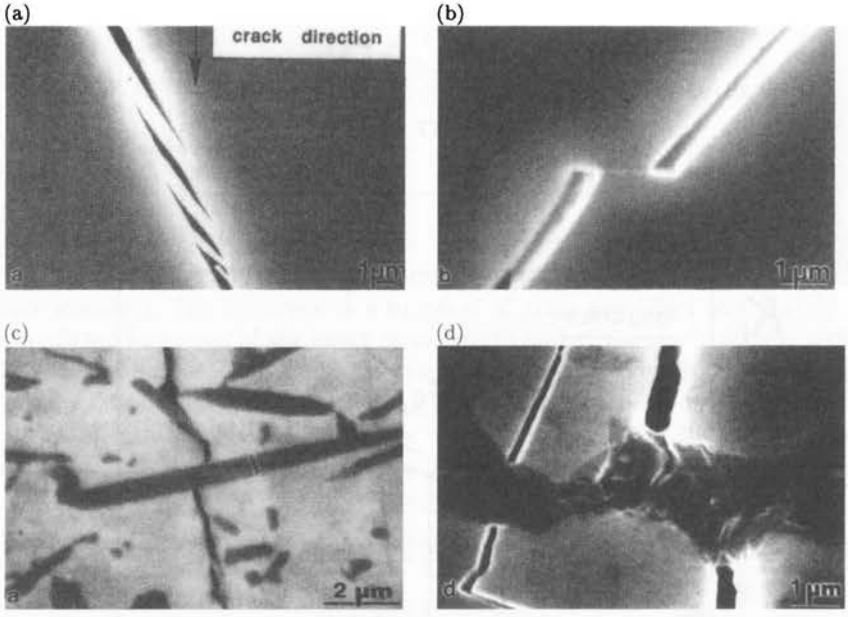

FIGURE 2. (a) elastic bridge in SiC; (b) frictional bridge in AL_2O_3; (c) interlocking in Al_2O_3/SiC_W; (d) ductile bridge in $Al_2O_3/SiC/Al$-composite [2].

The mechanical description allows a generalisation for the different materials. Please note that a single bridge can change it's mechanical effect by increasing the load (Fig. 3).

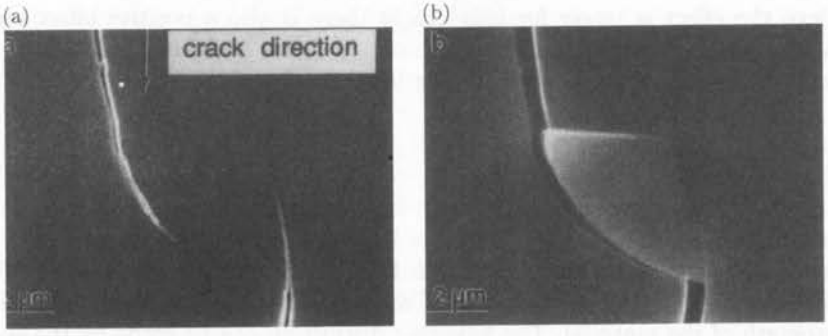

FIGURE 3. Bridge in Al_2O_3 from an elastic bridge (a) to a frictional bridge (b) [2].

2.2. Fibre reinforced materials

Fibre reinforcement can be subdivided into two groups:

1. In the case of a weak boundary between fibre and matrix the fibre debonds partially and is able to sustain high stresses. By calculating the force equilibrium (tensile stresses in the fibre are transferred by frictional stresses into the matrix) it is possible to evaluate the crack closure stresses of the fibres and the absorbed energy until fracture R_μ (compare Fig. 4). This leads to the following equations:

$$p(u) = \frac{2\,f\,E}{E_m(1-f)}\sqrt{\frac{\tau E_f}{R}}\sqrt{u},$$
$$R_\mu = \left[\frac{E}{E_m(1-f)}\right]^2 \frac{\sigma_f^3\,R\,f}{E_f\,6\tau}, \tag{2.1}$$

where:

E – Young's modulus,
E_f – Young's modulus of the fibre,
E_m – Young's modulus of the matrix,
f – volume fraction of fibres,
u – half crack opening displacement,
$p(u)$ – closure stress,
R_μ – energy absorbed until fibre fracture,

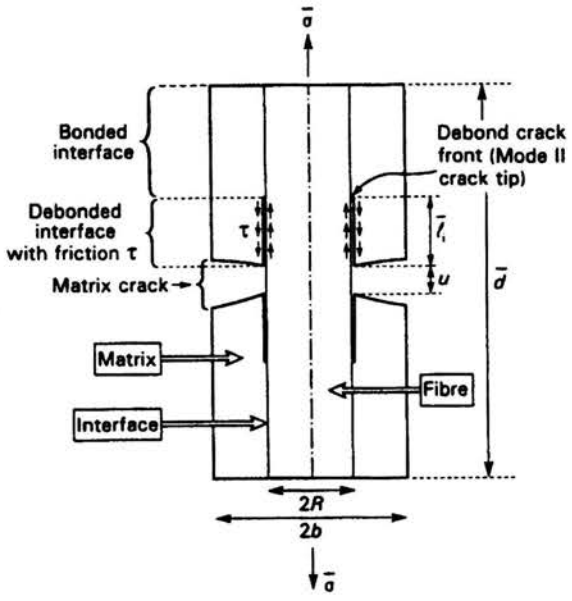

FIGURE 4. Description of the parameters in order to calculate R_μ in fibre reinforced materials [3].

σ_f – fracture strength of the fibre,
τ – frictional shear stress,
R – radius of the fibre.

2. After the fibre is broken (in most cases not between the crack faces) the fibre has to be pulled out of the matrix which is called "pull out". In this case the closure stress is:

$$p(u) = \frac{2\tau}{R}(h - u), \tag{2.2}$$

where:

h – distance between crack plane and position of the fibre fracture.

The typical stress-strain curve for fibre reinforced materials can be seen in Fig. 5:

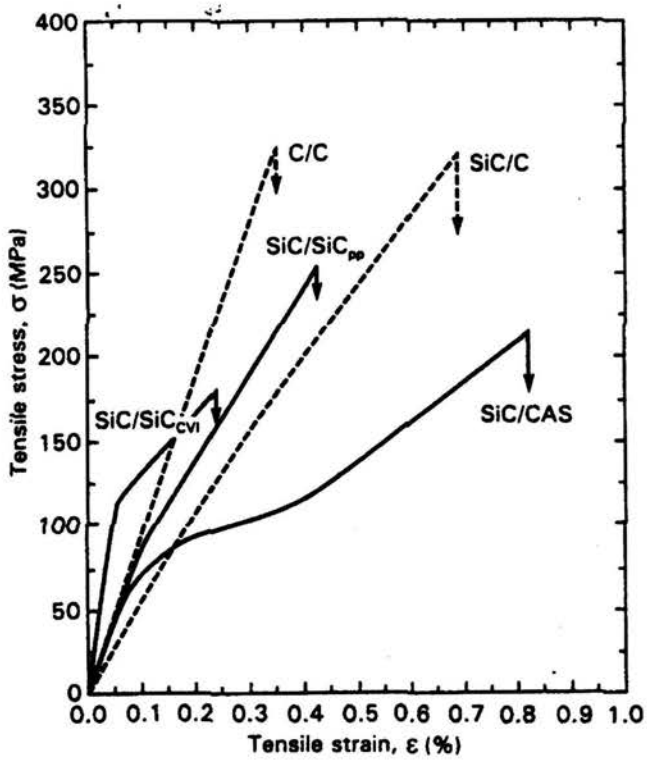

FIGURE 5. Stress-strain curve for different two dimensional CMC materials [3].

Perhaps the most important property of fibre reinforced materials is their high notch strength. In a normalised form this is shown in Fig. 6.

Typical values of C-fibre and SiC-fibre reinforced glasses are shown in Table 1. In the fabrication process of glasses fibre reinforced materials are used, for example as rollers, position markers etc.

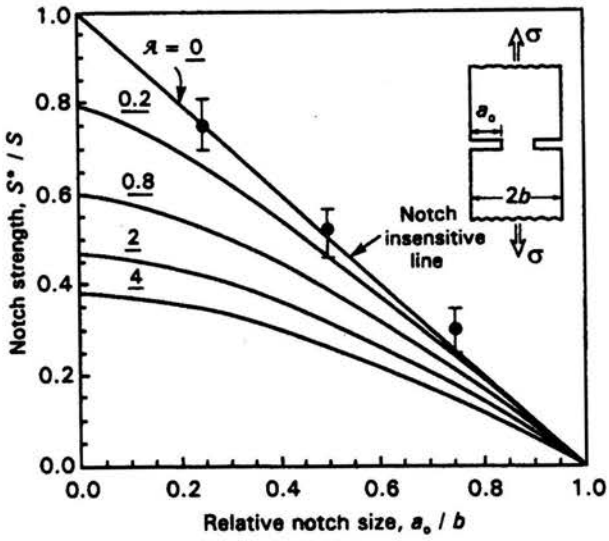

FIGURE 6. Experimental results to show the notch strength for a SiC/glass-ceramic [3].

TABLE 1. Characteristic values for fibre reinforced glasses.

Property	Fibre/matrix-combination	
	C-fibre/DURAN	SiC-fibre/SUPERMAX
ρ [g/cm^3]	1.9-2.2	2.3-2.5
σ_B [MPa]	700-1300	600-1100
E [GPa]	150-300	120-150
Weibull modulus m	20-30	20-30
α [10^{-6} K]	0-1	2-4
Thermal shock resistance [K]	> 500	> 500
Maximum temperature limit in oxidising atmosphere [°C]	$\geqslant$ 450	$\geqslant$ 700
λ [W/Km]	1-15	1.5-3

2.3. Whisker reinforcement

Since 1984 whisker reinforced ceramics are investigated. Most common are SiC-whisker in an Al_2O_3 matrix. Since it is known that whiskers can cause cancer the production process is under stringent safety conditions. This caused a price increase for whiskers which lead to a decrease in the use of this reinforcement material. The fabrication is done by hot pressing.

With a volume fraction of 5 to 20% whisker content in Al_2O_3/SiC_W – the compound has a fracture strength σ_B of 400-800 MPa and a fracture toughness K_{Ic} of 4-8 MPa$\sqrt{m}$. The possible toughening mechanisms are shown in Figs. 7, 8 and 9.

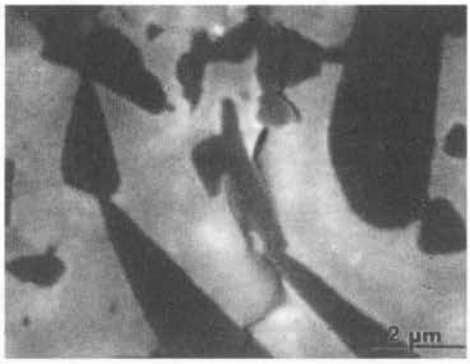

FIGURE 7. Whisker bridge 10 μm from the crack tip [2].

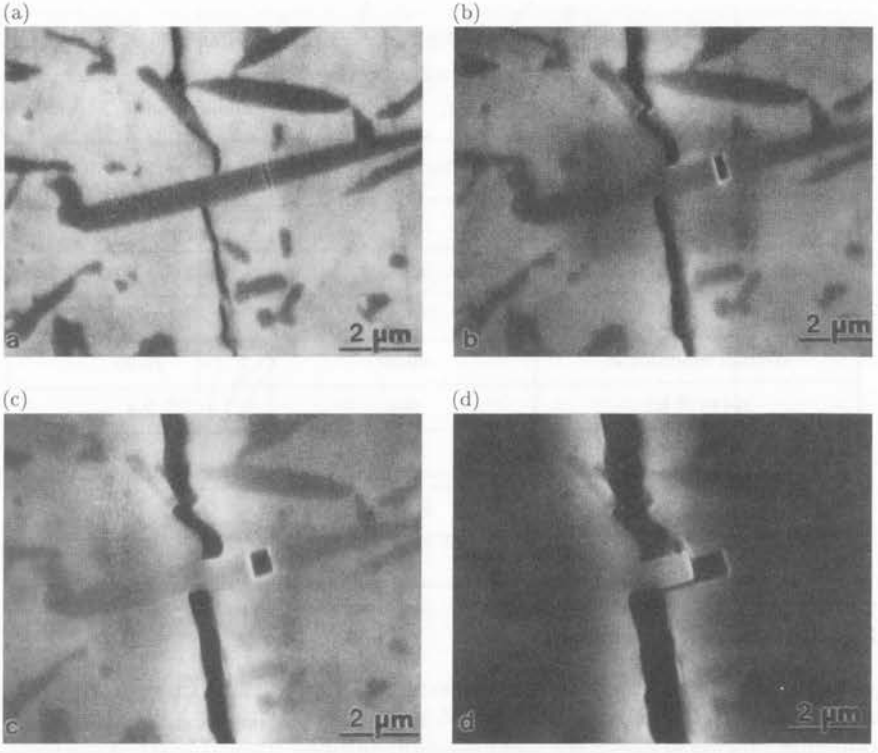

FIGURE 8. Whisker bridges: a) 100 μm, b) 110 μm, c) 330 μm, d) 830 μm distant from the crack tip [2].

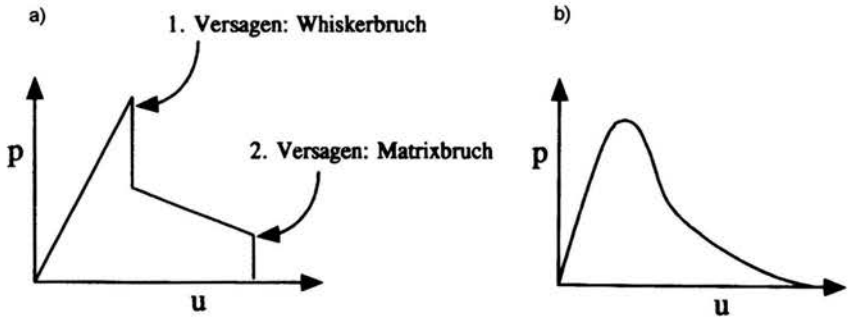

FIGURE 9. Schematic illustration of the $p(u)$-function for: a) an average whisker bridge with $\alpha = 90°$, b) the bulk material [2].

Materials with whiskers that are orientated transversely to the crack fail because of the fracture of the whisker and the matrix. The so called in-situ whisker toughening can be described similarly to the normal whisker toughening. In this case the processing is controlled so that columnar grains grow out of the matrix material. A well known example is Si_3N_4.

At the end of the 1980s materials were toughened by plates because of the carcinogenity of whiskers. The toughening with platelets showed little success. The reason was the weak interface between matrix and platelet which caused delamination which lowered the fracture toughness.

2.4. Particle toughening

Particle toughening is partly used to enable microcrack toughening (Sec. 3.3) or transformation toughening (Sec. 3.1). However particles are not suitable to bridge the crack, as they provide only a small elongation.

Another possibility for toughening is to incorporate fluctuations of residual stresses into the matrix in order to get complex crack patterns (Fig. 10). This leads

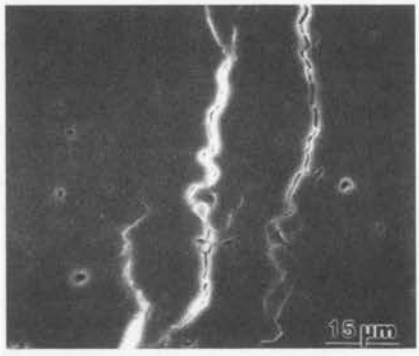

FIGURE 10. Crack extension in an Al_2O_3/Al_2TiO_5-composite material [2].

to crack bridging and crack branching. This concept, however, was not realised in a practical application.

A special kind of particle reinforcement was suggested by Niihara: nanotoughening. This term describes materials with nano particles (mostly SiC) of the size 50-200 nm incorporated into a microcrystalline matrix (mostly Al_2O_3). Even if the fracture toughness of these materials is only $K_{Ic} = 3\,\mathrm{MPa}\sqrt{\mathrm{m}}$ they show high fracture strengths of up to 1.5 GPa. The responsible mechanism for the strength increase is not clarified yet. These materials also show a high resistance against creep and abrasion.

2.5. Ductile toughening

By incorporating metal particles into the matrix a ductile bridge can be formed. Examples are hard metals like WC/Co (with σ_f up to 4 GPa and K_{Ic} up to $15\,\mathrm{MPa}\sqrt{\mathrm{m}}$) and Al_2O_3/Al. The interaction between crack and microstructure will be examplified by the pictures presented in Fig. 11.

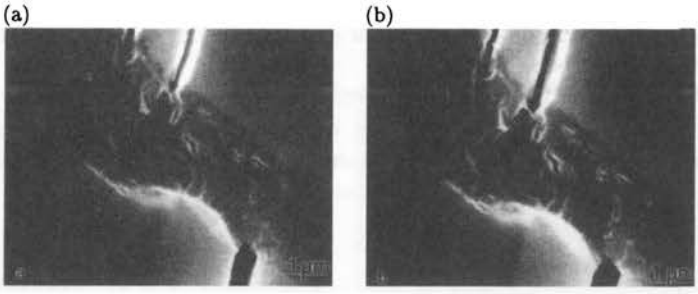

FIGURE 11. Crack extension in a SiC/Al_2O_3/Al-composite made by directional melt oxidation [2].

In addition to the influence of the diameter of the metal ligament (Fig. 12) there is also an influence of the interface strength on the $p(u)$-function which results in different R-curves (Fig. 13).

3. Process zone mechanism

3.1. Transformation toughening

3.1.1. The fracture toughness approach. In 1975 Garvie et al. [9] first described transformation toughening in ZrO_2. This was the beginning of deeper research into the field of transformation toughening as a possibility to increase fracture toughness. In 1981 McMecking and Evans [10] proposed a model to describe this phenomena solely by the dilatational strains which are a result of the volume expansion during the transformation. Other models were introduced over the years like the one by Chen which also includes the shear strains of the transformation [11]. Lately Hannink et al. [12] provided a review of the current understanding.

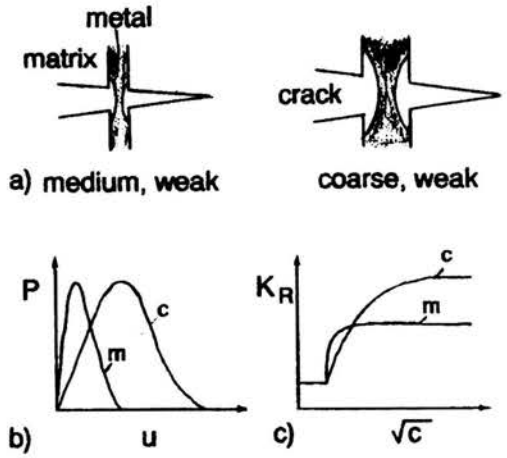

FIGURE 12. Schematic illustration of (b) $p(u)$-functions and (c) R-curves for metal infiltrated ceramics with (a) different ligament diameters assuming size independent metal deformation [4].

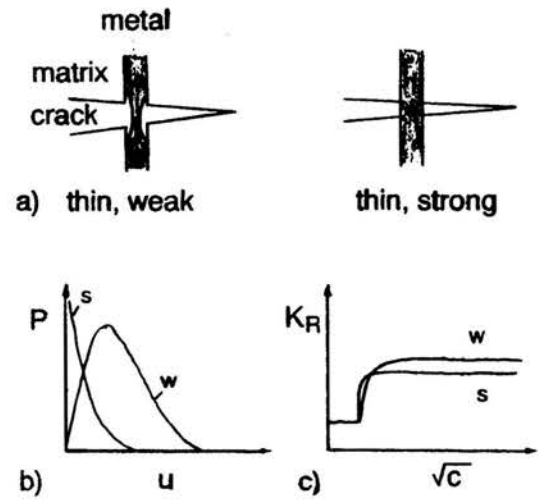

FIGURE 13. Schematic illustration of (b) $p(u)$-functions and (c) R-curves for (a) weak and strong interfaces [4].

Requirement: Phase transformation with volume increase during cooling, for example

$$ZrO_2: \quad c \xrightarrow{2360°C} t \xrightarrow{1200°C} m$$

$t \longrightarrow m$ – martensitic transformation at M_s, displacive, without time delay, $\Delta V = 4\%$,
$M_s = f(d, c_{Dot}, p)$ – martensitic temperature.

The tetragonal phase can be stabilised at room temperature with dopands or by decreasing the grain size.

Goal: The microstructure is stable if no load is applied. The phase transformation takes place when a tensile stress is applied.

K-formulation: The transformation takes place if a certain hydrostatic stress σ_h is applied:

$$\sigma_h = \frac{1}{3}(\sigma_1 + \sigma_2 + \sigma_3). \tag{3.1}$$

σ_m^c is the critical minimum stress so that the transformation takes place.

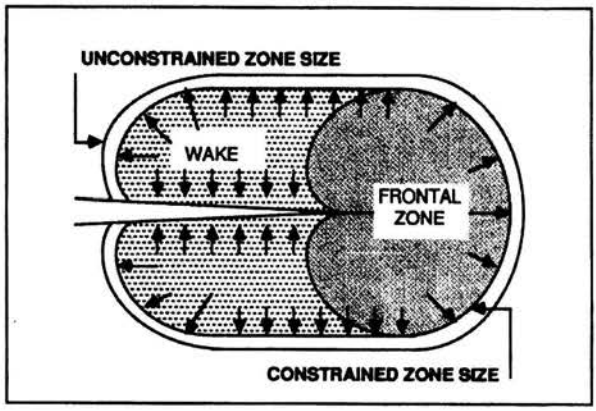

FIGURE 14. Schematic illustration of the stress field in a dilatational transformation zone [5].

For the zone in front of the crack tip the increase in the fracture toughness due to the transformation is $K_\mu = 0$. At an angle of $\theta = 60°$ the height h of the transformation zone reaches its maximum. The size and shape of the transformation zone is given by :

$$r_T(\theta) = \frac{2(1+\nu)^2}{9\pi}\left(\frac{K_I}{\sigma_m^c}\right)^2 \cos^2\left(\frac{\theta}{2}\right), \tag{3.2}$$

where:

r_T – radius of the transformation zone,
θ – angle between the extended crack plane and the considered volume element,
ν – Poisson's ratio,
K_I – stress intensity factor,
σ_m^c – critical transformation stress.

For the amount of toughening increase the height h of the plastic zone is important:

$$h = \frac{\sqrt{3}(1+\nu)^2}{12\pi}\left(\frac{K_I}{\sigma_m^c}\right)^2, \tag{3.3}$$

where:

h – height of the transformation zone.

The integration of the compressive stresses for an infinite crack gives:

$$K_\mu = 0.21\, E V \varepsilon^T \frac{\sqrt{h}}{(1-\nu)}, \tag{3.4}$$

where:

E – Young's modulus,

V – volume,

ε^T – volume strain during phase transformation.

The shielding term is dependent on the crack length Δc:

$$K_\mu(\Delta c) = E V \varepsilon^T \sqrt{h} f\left(\frac{\Delta c}{h}, \nu\right). \tag{3.5}$$

In Fig. 15 the dependence of the toughening on the crack length is shown. This leads to the R-curve in Fig. 16. The maximum of toughening is reached when the crack length is approximately five times the height of the transformation zone.

As an example K_μ is calculated for a typical Y-TZP-ceramic:

$$K_I = 2\,\mathrm{MPa}\sqrt{\mathrm{m}}, \quad h = 10\,\mu\mathrm{m}, \quad \nu = 0.25,$$

$$\sigma_m^c = \frac{K_I}{\sqrt{h}}\sqrt{\frac{3(1+\nu)^2}{12\pi}}, \tag{3.6}$$

$$\Rightarrow \quad \sigma_m^c = 320\,\mathrm{MPa}, \quad K_{\mu,\max} = 5\,\mathrm{MPa}\sqrt{\mathrm{m}}.$$

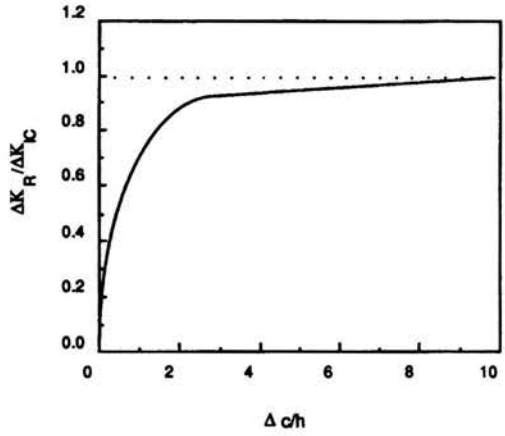

FIGURE 15. Increase of toughness with increasing crack length [5].

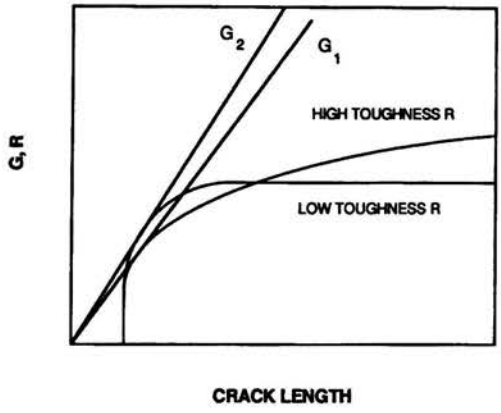

FIGURE 16. R-curve for two ceramics with a different maximum fracture toughness [5].

The effective height h of the transformation zone can be measured experimentally by:

- Nomarski-interference,
- Raman-spectroscopy,
- AFM (atomic force microscope).

The amount of transformed material can be characterised by XRD or Raman measurements on the fracture surface.

To achieve a high toughening effect the zone height h has to be big. But it has to be less than the dimensions of the sample. However if σ_m^c is too small the material transforms prematurely without tensile stresses or without a crack.

3.1.2. The mechanical energy release rate approach. We have

$$R_\mu = 2 \int_0^h u(y) dy, \tag{3.7}$$

where:

R_μ – fracture energy, consumed in the process zone,
$u(y)$ – remaining elastically stored energy due to the transformation,
ε^T – volume strain during phase transformation.

For the transformation it follows:

$$R_\mu = 2 \sigma_m^c V \varepsilon^T h. \tag{3.8}$$

These results are consistent with the K-description.

Figure 17 shows the stress-strain curve for a material with a dilatational phase transformation.

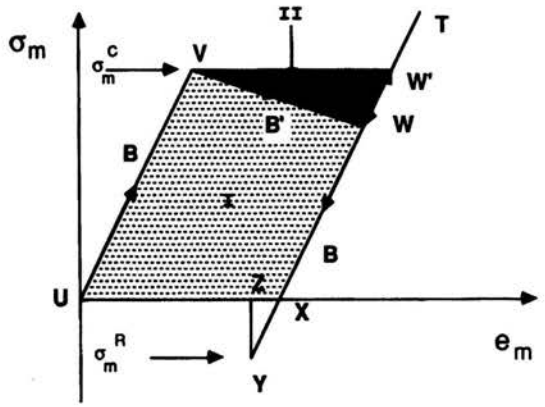

FIGURE 17. Relation between hydrostatic stress and volumetric strain for a material with a tensile stress induced phase transformation [5].

The medium compressive stress σ_m^R is:

$$\sigma_m^R = \frac{-2\,E\,V\,\varepsilon^T}{9(1-\nu)}. \tag{3.9}$$

3.1.3. Effects. In materials with transformation toughening failure is limited by the constant inherent flaw size given by the Griffith equation. After reaching a maximum the fracture strength decreases with increasing fracture toughness because the limiting factor has changed. Now the failure is limited by the yield stress or in other words plasticity is limited (Fig. 18).

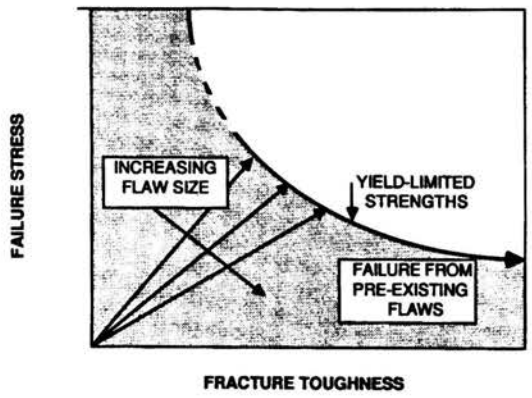

FIGURE 18. Schematic illustration of the relation between fracture toughness and fracture strength in transformation toughened ceramics [5].

3.2. ZrO_2-materials

Generally three zirconia materials are distinguished:

- PSZ – **P**artially **S**tabilised **Z**irconia (cubic ZrO_2 matrix; tetragonal ZrO_2 precipitates),
- TZP – **T**etragonal **Z**irconia **P**olycrystal (only tetragonal ZrO_2),
- ZTA – **Z**irconia **T**oughened **A**lumina (Al_2O_3 matrix; tetragonal ZrO_2 precipitates).

PSZ

Typical dopants are MgO and CaO. Figure 19 shows the phase diagram of Mg-PSZ (magnesia stabilised PSZ)

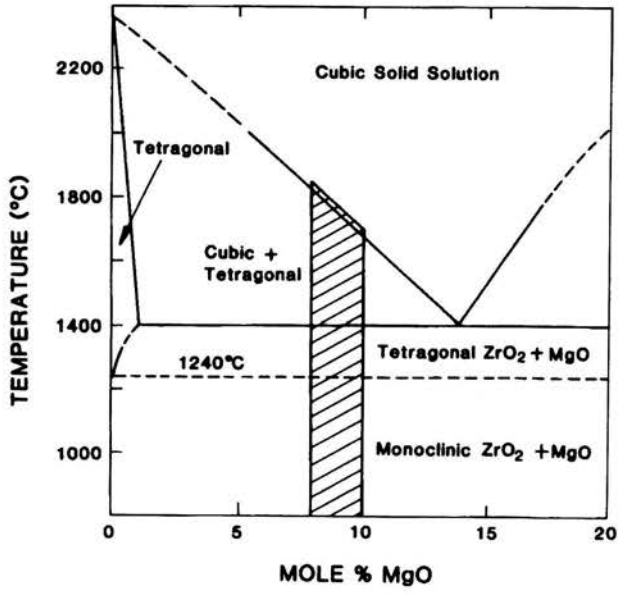

FIGURE 19. Phase diagram for Mg-PSZ [5].

The fabrication includes the following steps:

1. sintering in the cubic phase field,
2. rapid cooling,
3. tempering above the eutectic temperature in order to get tetragonal precipitates.

A typical microstructure can be seen in Fig. 20.

The size of the lenticular precipitates determines the mechanical properties (Fig. 21). Small precipitates have a higher σ_m^c. Therefore less material is transformed at a given applied load. The height h of the transformation zone determines

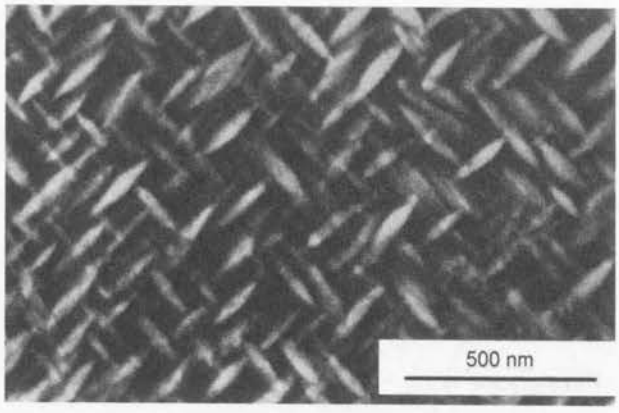

FIGURE 20. Microstructure of Mg-PSZ [5].

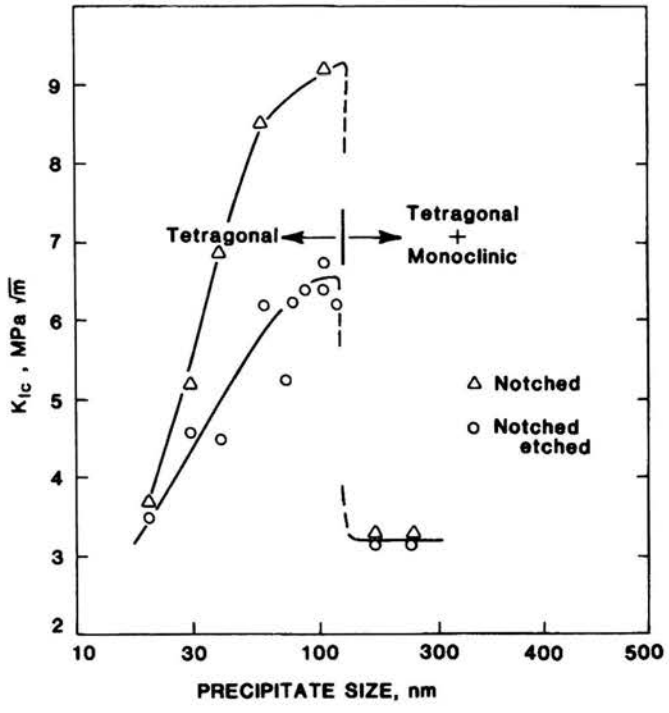

FIGURE 21. Influence of the precipitate size on K_{Ic} for Ca-PSZ [5].

the increase in fracture toughness. Since a low σ_m^c means a high h, K_{Ic} increases with increasing precipitate size. But there is an upper limit. If the precipitate size reaches a certain size (in Fig. 21 for this material $\sim 150\,\text{nm}$) the precipitates transform spontaneously without an applied load and the fracture toughness decreases.

TZP

Typical dopants are Y_2O_3 and CeO_2. The zirconia rich side of the Y_2O_3-ZrO_2 phase diagram is shown in Fig. 22.

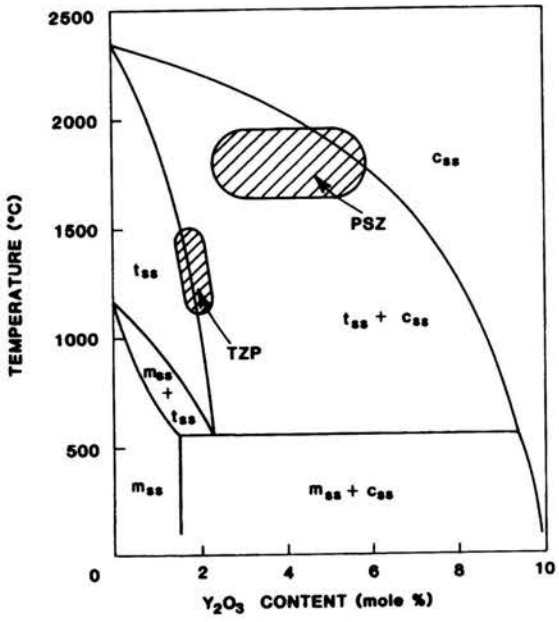

FIGURE 22. Phase diagram Y_2O_3-ZrO_2 [5].

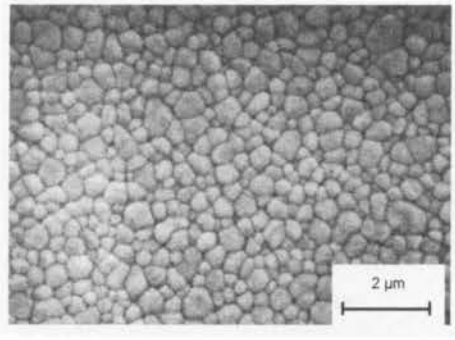

FIGURE 23. Microstructure of Y-TZP [5].

Y-TZP contains typically 2-3.5 mol-% Y_2O_3 and is sintered at 1400°C. A typical microstructure can be seen in Fig. 23.

The mechanics can be controlled by the Yttria content (K_{Ic} increases with decreasing Yttria content, Fig. 25) and the grain size (K_{Ic} increases with increasing grain size, Fig. 26). The fracture strength does not necessarily increase with increasing K_{Ic} (Fig. 24).

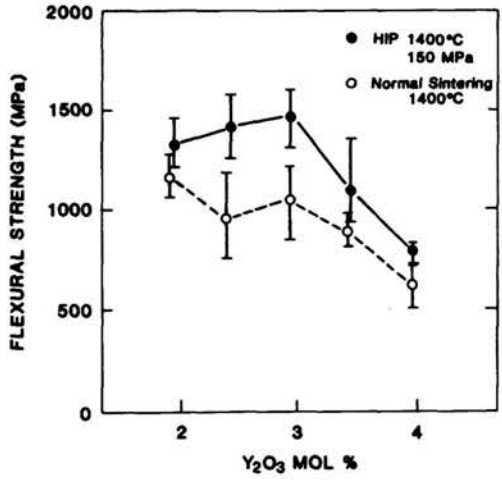

FIGURE 24. Flexural strength dependence on Y_2O_3 content of sintered and hot isostatically pressed (HIP) Y-TZP materials [5].

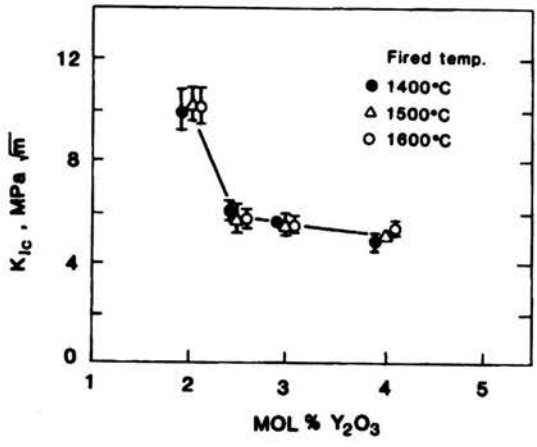

FIGURE 25. Fracture toughness measured using Vicker's indentation technique for Y-TZP materials as a function of Y_2O_3 content and sintering temperature [5].

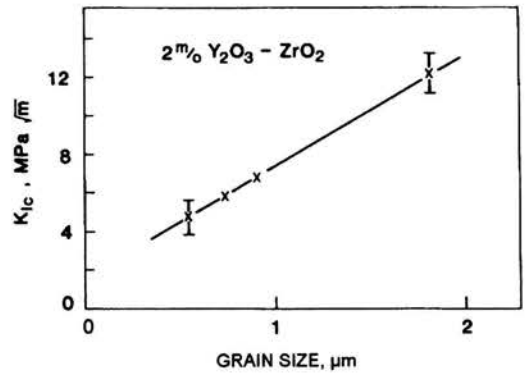

FIGURE 26. Grain size dependence of the fracture toughness [5].

ZTA

Figure 27 shows a typical SEM picture of the microstructure for a ZTA material with the bright t-ZrO_2 phase and the dark Al_2O_3 matrix.

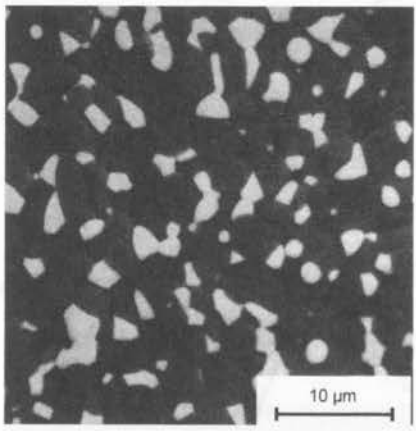

FIGURE 27. Microstructure of a ZTA-composite material [5].

ZTA is toughened by two mechanisms:

- transformation toughening,
- microcrack toughening.

3.3. Microcrack toughening and materials

Microcrack toughening is similar to transformation toughening. In the case of a microcrack the extra volume is created by the microcrack and this extra volume

creates a closure stress:

$$K_\mu = 0,21\, E\, \varepsilon_{mc}\, \frac{\sqrt{h}}{(1-\nu)}, \tag{3.10}$$

where:

E – Young's modulus,
h – height of the plastic zone,
ν – Poisson's ratio,
ε_{mc} – strain, caused by micro crack.

Since microcracking decreases the Young's modulus, the slope of the unloading curve of the representative volume element in front of the crack tip is lower compared to the loading curve (Fig. 28).

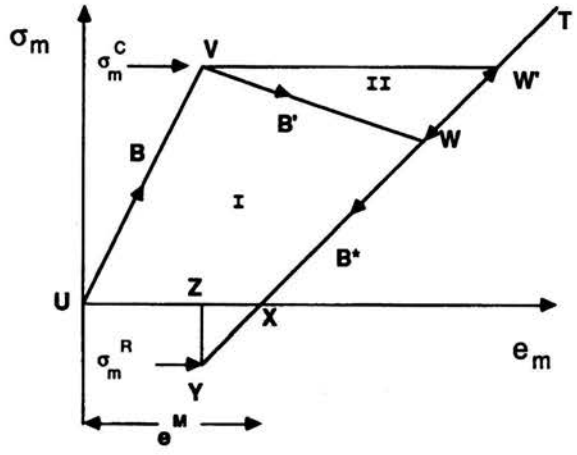

FIGURE 28. The mean stress-volumetric strain behaviour for an element of constrained material subject to a supercritical microcracking [5].

Microcracking as a toughening mechanism is only proven in a few materials like ZTA and SiC/TiB_2. The significance is much lower than that of transformation toughening.

3.4. Ferroelastic toughening

Ferroelastic behaviour is based on the switching of domains. This leads to an extra strain in the direction of the applied stress.

Since the switching of the domains determines the toughening effect, the initial orientation of the domains has an influence on the amount of ferroelastic toughening. This can be demonstrated by measuring the R-curves of PZT poled into the three directions and by comparing this with an unpoled material (Fig. 30).

The piezoelectric effect causes crack shielding at the crack tip. After unloading the toughening effect vanishes with time because the domains switch back into their original position.

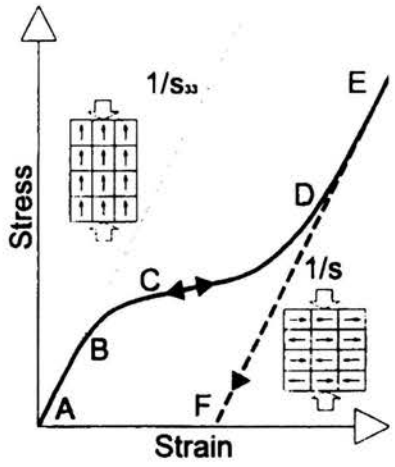

FIGURE 29. After a linear increase most of the domains switch. After most of the domains have switched the stress-strain curve is linear again. After unloading there is a residual strain [6].

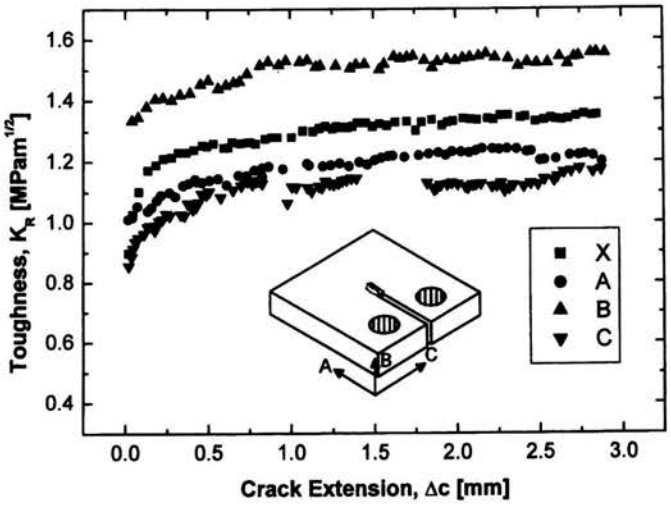

FIGURE 30. R-curve for a PZT poled in different directions [7].

3.5. Materials exhibiting ferroelastic toughening

The most important materials ($BaTiO_3$, PZT) belong to the crystallographic class of perovskite (Fig. 31). PZT is commercially used as an actuator and as a sensor (load cell).

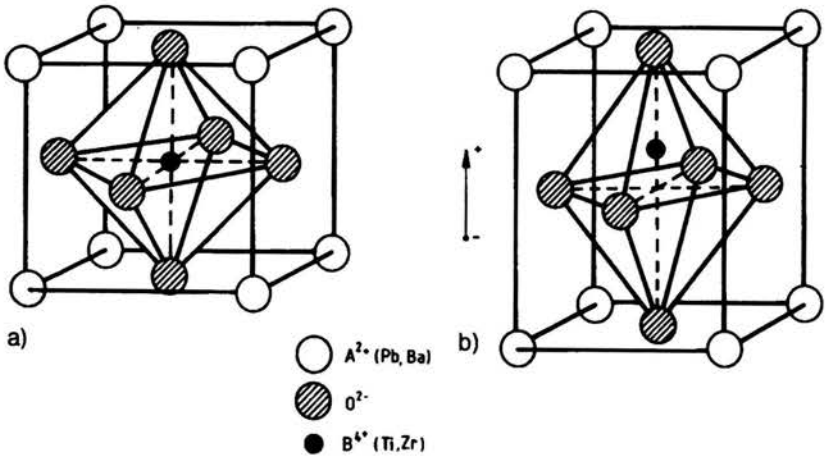

FIGURE 31. Unit cell of a perovskite: a) cubic lattice above Curie-temperature b) tetragonal lattice below Curie-temperature [8].

II. Fracture of ceramics

II.A. Fracture of Alumina as a function of grain size

4. Introduction

Extensive investigations of the fracture surfaces of polycrystalline ceramics, especially alumina, have shown that fracture invariably originates from some form of pre-existing defect [16, 17]. These pre-existing defects may arise from imperfect processing, such as a pore or an inclusion, may result from specimen handling, or, may be intrinsic in nature, such as a microcrack at grain boundaries as a result of thermal expansion anisotropy. Grain size also has a clear effect upon the fracture strength of alumina [18-21]. Despite this knowledge, a clear consensual understanding of the processes involved in the fracture of polycrystalline ceramics has not been obtained. It is the aim of this study to assist in elucidating the factors involved in the fracture of alumina and other polycrystalline ceramics.

The relationship between the fracture strength and grain size of polycrystalline ceramics is often represented in the form of an Orowan-Petch plot, which plots fracture strength versus the inverse square root of the average grain size, as shown schematically in Fig. 32. As seen in Fig. 32 the plot is divided into two regimes: the Orowan regime which describes the behaviour of coarse grained materials and the Petch branch which describes the behaviour of fine grained materials. The Orowan branch shows a strong increase in fracture strength with decreasing grain size [18]. Conversely, the Petch branch, shows that for fine grained materials fracture strength increases only slightly [19-21] or remains constant [22] with decreasing grain size. In alumina the transition from Orowan to Petch behaviour [23, 24] occurs at an average grain size in the region of 5-15 μm.

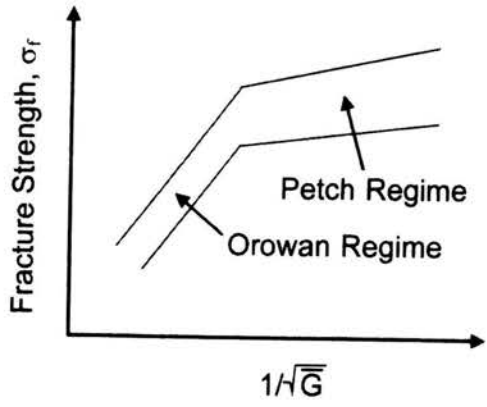

FIGURE 32. Schematic representation of the Orowan-Petch relationships between fracture strength, σ_f, and the inverse square root of the average grain size, $1/\overline{G}$ [13].

A number of proposals exist in the literature to explain the effect of grain size upon strength in polycrystalline ceramics. One proposes that a local fracture toughness variation exists in going from fracture initiation in a single crystal to fracture initiation in a polycrystal structure leading to a reciprocal square root law for grain size dependence [25]. Another explains the dependence in terms of variations in the R-curve with grain size [24]. Fracture in the Orowan regime is predicted to occur when a critical point is reached on the R-curve and is relatively insensitive to the size of the failure origin, be it extrinsic or intrinsic. As grain size decreases and hence R-curve behaviour, the fracture strength becomes governed by extrinsic flaws and displays a Petch regime behaviour [24].

A recent work, involving extensive fracture origin analysis, was successful in quantitatively modelling the grain size dependence of the fracture strength in the Petch regime [17]. The combination of either a spherical pore with a circumferential crack or a hemispherical surface pit with a peripheral crack could rationalize a drop in fracture strength from 564 MPa at 1.7 μm grain size to 320 MPa at 11 μm grain size. Crack closure stresses of 120 MPa were shown to have a minute influence on strength, as well as strength variability [17].

Crack closure stresses have been determined by various investigators for a range of alumina materials with results for the peak closure stress ranging from 17 to 120 MPa. A robust method with high resolution is based on measurement of crack opening displacements close to the crack tip combined with the use of a weight function concept [26]. This concept was applied to alumina in the Petch regime with grain sizes ranging from 1.7 μm to 10.5 μm [26]. Closure stresses were found not to exceed 20 MPa for all grain sizes. Preceding attempts overestimated the magnitude of closure stresses, because monotonically decreasing laws of closure stresses as a function of crack opening were assumed and the maximum at crack opening u=0 was extrapolated from long crack measurements [27, 28]. Additionally, the crack tip toughness, or the intrinsic material toughness, was found to be independent of grain size [29], equal to 2.3 MPa$\sqrt{\text{m}}$. Crack closure stress data for alumina of grain sizes in

the Orowan regime show levels of crack closure stress up to 50 MPa [30]. However, even assuming these high closure stresses, bridging interactions have limited effect on the critical stress of failure from pores [17].

The objective of the current study is to identify a stress concentrator as well as the ensuing crack geometry at final fracture. This knowledge allows assessment of the influence of grain size on crack dimensions. Finally, this leads to a prediction of fracture strength as a function of grain size.

The approach is distinguished by a combination of refined microstructural control, extensive fractographic analysis and detailed fracture mechanics computation. Microstructures with equiaxed grain sizes in the range of 0.8 to 9.2 μm size were produced with embedded spherical pores of 85 μm diameter. Defect origins were then defined by fractography and two possible crack configurations (semicircular crack and circumferential crack) were considered. Surface correction terms in conjunction with the stress concentrating effect of the pore were utilized to describe the evolving crack instability upon loading. An inclusion of the peak closure stress in the crack resistance term proved that use of a single valued crack tip toughness is sufficient to describe crack equilibrium.

5. Model

5.1. Description of the model

5.1.1. Geometrical description. Based on fractographic evidence [17, 31], a model for brittle fracture has to include the interaction of two different defect populations. Intrinsic defects on a microstructural level such as grain boundaries have to be considered as nucleation sites for microcracks, whereas processing defects such as pores or inclusions, act as stress concentrators. In this work, one specific type of stress concentrator, namely a spherical pore intersecting the sample surface, is combined with various crack geometries. Residual stresses are assumed as a driving force for microcrack formation, although their influence on crack instability is neglected. This is acceptable as an approximation, because residual stresses on a microstructural level change their sign randomly, thus alternating between tension and compression. Microstructural influence in principle is exerted in form of a crack tip toughness and by closure stresses due to crack bridging. In the case of alumina, crack tip toughness was found to be independent of grain size, at least as far as the grain size regime between 0.8 and 11 μm is concerned [29]. Because lack of better data, we therefore utilize a grain size invariant crack tip toughness in our model. For many ceramics, average closure stresses are not relevant for strength predictions, since the applied stress intensity factor is rising much faster with increasing crack length than the contribution to crack resistance due to bridging effects for realistic assumptions of crack shape and size at criticality [17]. In general terms, as long as closure stresses are small compared to strength, their influence can be neglected, as considered in this work. Grain size exerts an influence on strength, because the starter crack length and for the lack of stable crack growth also the crack length at instability for fracture from a fixed stress concentration site such as a spherical pore is scaling with grain size. Thus, the critical crack length, c, is correlated with grain size.

The conditions outlined above are cast into three different models as sketched in Fig. 33. Their common feature is a location at the edge of a spherical pore. The semicircular crack emanating from the pore in Fig. 33b can be considered as the most realistic description of cavity fracture [32], but the applicability of this model is limited to crack lengths which are small compared to the pore radius. Therefore, envelopes for the real behaviour are chosen with the circumferential crack [32-38] in Fig. 33a forming one extreme with the crack tip line seeing the highest effect of the stress concentrator, while the circular crack in Fig. 33c constitutes the opposite envelope with the crack tip line seeing the least stress concentration at the maximum distance from the pore.

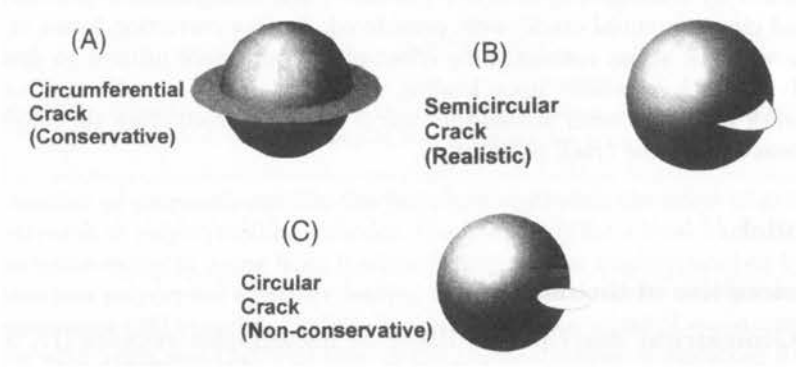

FIGURE 33. Schematic 3-dimensional representation of (a) circumferential, (b) semicircular and (c) circular crack emanating from a spherical pore [14].

Assessment of stress intensity factors is divided into two subsections. First, the stress distribution of the uncracked configuration is derived by means of elasticity theory. In a second step, the elastic stress distribution is integrated over the respective crack area utilizing the weight function approach.

5.1.2. Stress distributions. In order to stress a balance between applicability and mathematical tractability we chose a spherical pore intersecting at the midplane the tensile surface of a specimen being subjected to biaxial flexure. The selection of a hemispherical pore is based on the observation that fracture originates from pores intersecting the surface with a degree of embedding ranging from half to almost complete [13]. In this configuration, the stress concentration is maximized at the bottom of the pore. Via finite element modelling it can be demonstrated that the stress distribution at the bottom is virtually identical for all spherical pores which exhibit an intersection with the surface [13]. Since pore size is small in comparison to specimen dimensions, the applied far field stress can be considered as constant, effectively reducing biaxial flexure to biaxial tension. The maximum tensile stress in

a material with Poisson's ratio $\nu = 0.25$ under biaxial load around a hemispherical pore at a free surface as a function of distance is given by Eq. (5.1a) [13, 37a]:

$$\sigma = \sigma_A \left[1 + 1.153 \left(1 + \frac{r}{R}\right)^{-5} + 7.968 \cdot 10^{-2} \left(1 + \frac{r}{R}\right)^{-3}\right]. \qquad (5.1a)$$

Here σ_A denotes the applied far field stress, R – the pore radius and r – a radial distance from the pore. The stress distribution of a hemispherical pore may be contrasted to the stress field of a spherical pore subjected to biaxial tension (Eq. (5.1b)) in Fig. 34. Poisson's ratio is, again, chosen as $\nu = 0.25$. It is apparent that the difference between both stress concentrators is only slight and the basic physical principles will not be affected by the particular geometry chosen. Additionally, it was recently demonstrated that the solution according to Eq. (5.1a) might show a certain error, i.e. the stress concentration factors of both configurations might be almost identical [37b], see formula (5.1b) below,

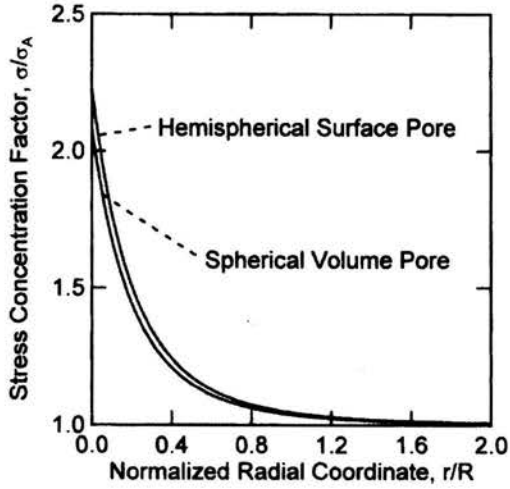

FIGURE 34. Stress concentration around an embedded spherical pore as compared to stress concentration at the bottom of a hemispherical pore at the specimen surface (Poisson's ratio $\nu = 0.25$).

TABLE 2. Numerical Coefficients for Eq. (5.1b).

Poisson's ratio ν	A	B
0.2	1	0
0.25	1.043	$4.348 \cdot 10^{-2}$
0.3	1.091	$9.091 \cdot 10^{-2}$

$$\sigma = \sigma_A \left[1 + 1.043 \left(1 + \frac{r}{R}\right)^{-5} + 4.348 \cdot 10^{-2} \left(1 + \frac{r}{R}\right)^{-3}\right]. \tag{5.1b}$$

Numerical coefficients for Eq. (5.1b) are given in Table 2 for other values of Poisson's ratio.

5.1.3. Stress intensity factors. The stress distribution of a hemispherical pore is used for all three models, while the weight function, h, depends on the assumed crack geometry. In principle, calculation of the applied stress intensity factor, K, is based on Eq. (5.2) [38]:

$$K = \int_0^c h(r, c)\, \sigma(r)\, dr. \tag{5.2}$$

Here, the crack length is denoted by c. The semicircular and circumferential crack configurations, have been treated in the literature and are therefore described only briefly here. The circular crack model will be derived in the next section.

The weight function for the circumferential crack (Fig. 35a), which serves as a conservative estimate, consists of two components. Depending on the normalized

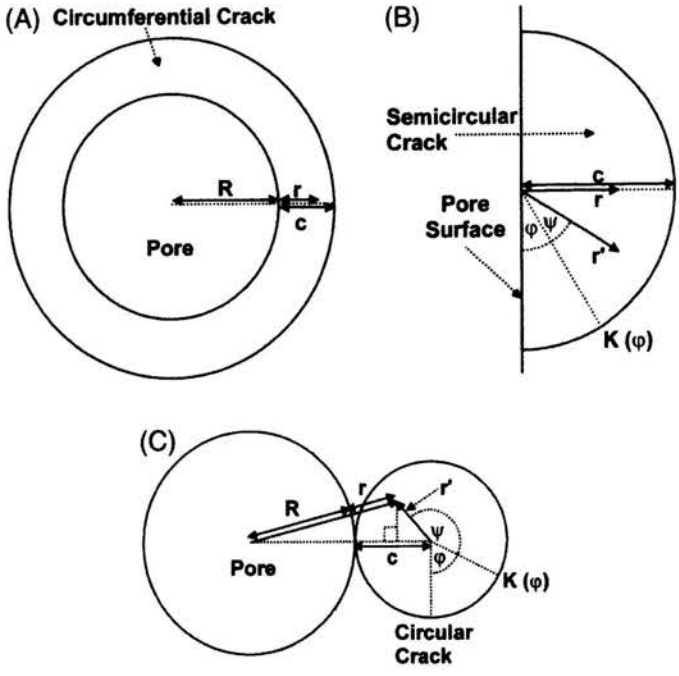

FIGURE 35. Schematic 2-dimensional representation of an intersection through the crack plane for: (a) circumferential, (b) semicircular and (c) circular crack model. The coordinate systems and nomenclature used for modelling are also shown.

crack length c/R, the weight function h provides a transition between circular crack and edge crack [36]:

$$h = \beta\, h_{\text{edge crack}} + (1-\beta)\, h_{\text{circular crack}}. \tag{5.3}$$

Here, $h_{\text{edge crack}}$ and $h_{\text{circular crack}}$ denotes the weight function of an edge crack [39] or a circular crack [36], respectively, while β can be considered as an interpolation function:

$$\beta = \frac{1}{\left(1+2\frac{c}{R}\right)^2}. \tag{5.4}$$

The interpolation function β describes the correct limits, because $\beta = 1$ for $c/R \to 0$ and $\beta = 0$ for $c/R \to \infty$, thus representing a pure edge crack or circular crack. Equations (5.5) give the two relevant weight functions:

$$h_{\text{edge crack}} = \frac{2}{\sqrt{\pi c}} \frac{\left[1.3 - 0.71\left(\frac{r}{c}\right)^2 + 0.41\left(\frac{r}{c}\right)^3\right]}{\sqrt{1-\left(\frac{r}{c}\right)^2}}, \tag{5.5a}$$

$$h_{\text{circular crack}} = \frac{2}{\sqrt{\pi\,(c+R)}} \frac{(r+R)}{\sqrt{(c+R)^2-(r+R)^2}}. \tag{5.5b}$$

It has to be noted that the weight function given by Eq. (5.5b) is valid only for axisymmetric stress distributions. Combination of Eqs. (5.1) to (5.5) yields the stress intensity factor for the circumferential crack.

While the circumferential crack model is axisymmetric, this symmetry is lost for the other two models. Therefore, the stress distribution becomes a function of two variables, and the general weight function approach described by Eq. (5.3) has to be corrected by the introduction of a second integration variable. This step is performed in Eq. (5.6) which contains the weight function for circular cracks in a more general form than Eq. (5.5b) [39].

$$K(\varphi) = \frac{1}{\pi \cdot \sqrt{\pi c}} \cdot \int_0^{2\pi} \int_0^{c} \frac{\sigma(r',\varphi) \cdot r' \cdot \sqrt{c^2 - r'^2}}{c^2 + r'^2 - 2r'c \cdot \cos\psi} dr'\, d\psi \tag{5.6}$$

The angle φ defines the point along the crack tip line, for which the applied stress intensity factor, K, is evaluated, while ψ is a dummy variable. The semicircular and circular crack model are both derived via Eq. (5.6). Because the following steps are similar, both models are treated together. As sketched in Fig. 35b,c, the two configurations require the introduction of a new radial coordinate, r', since the local stress which is expressed in Eq. (5.1a) as a function of distance from the pore center has to be determined with respect to the distance from the center of the circular

crack. This coordinate substitution is provided in Eq. (5.7a) for the semicircular crack and in Eq. (5.7b) for the circular crack:

$$r = r' |\sin(\varphi + \psi)|, \tag{5.7a}$$

$$R + r = \sqrt{[R + c + r' \sin(\varphi + \psi)]^2 + [r' \cos(\varphi + \psi)]^2}. \tag{5.7b}$$

Combination of Eqs. (5.1a), (5.6) and (5.7a) or (5.7b), respectively, yields Eq. (5.8a) for the semicircular and Eq. (5.8b) for the circular crack model:

$$K(\varphi) = \frac{\sigma_A}{\pi\sqrt{\pi c}} \int_0^{2\pi} \int_0^{c} \left\{ 1 + 1.153 \left[1 + \frac{r' |\sin(\varphi + \psi)|}{R} \right]^{-5} + 7.968 \cdot 10^{-2} \left[1 + \frac{r' |\sin(\varphi + \psi)|}{R} \right]^{-3} \right\} \frac{r' \sqrt{c^2 - r'^2}}{c^2 + r'^2 - 2r' c \cos\psi} \, dr' d\psi, \tag{5.8a}$$

$$K(\varphi) = \frac{\sigma_A}{\pi\sqrt{\pi c}} \int_0^{2\pi} \int_0^{c} \left\{ 1 + \frac{1.153 R^5}{\left\{ [R + c + r' \sin(\varphi + \psi)]^2 + [r' \cos(\varphi + \psi)]^2 \right\}^{5/2}} + \frac{7.968 \cdot 10^{-2} R^3}{\left\{ [R + c + r' \sin(\varphi + \psi)]^2 + [r' \cos(\varphi + \psi)]^2 \right\}^{3/2}} \right\} \frac{r' \sqrt{c^2 - r'^2}}{c^2 + r'^2 - 2r' c \cos\psi} \, dr' d\psi. \tag{5.8b}$$

For the semicircular crack model, a simple surface correction method was used in order to incorporate the influence of the pore surface [40]. The surface correction is taken as the ratio of the stress intensity factor, $K_{c,s}$, for a semicircular surface crack under constant stress and the stress intensity factor, K_c, for an internal circular crack under constant stress. The stress intensity factor of the semicircular crack located at a pore including a surface correction, K_s, can then be calculated from the respective value without surface correction, K, from Eq. (5.8a):

$$K_s(\varphi) = K(\varphi) \frac{K_{c,s}(\varphi)}{K_c}. \tag{5.9}$$

The local stress intensity factor, $K_{c,s}$, for the semicircular surface crack under constant applied stress is contained in the empirical equations of Raju and Newman [41] as a special case of a semielliptical crack. In Eq. (5.10) an infinite specimen thickness was assumed:

$$K_{c,s}(\varphi) = \sigma_A \sqrt{c} \cdot 1.04 \cdot \sqrt{\frac{\pi}{2.464}} \left[1 + 0.1 (1 - \sin\varphi)^2 \right]. \tag{5.10}$$

The stress intensity factor for an internal, circular crack in an infinite specimen under constant, applied stress is given by Eq. (5.11):

$$K_c = \frac{2}{\sqrt{\pi}} \sigma_A \sqrt{c}. \tag{5.11}$$

Since the circular crack model is considered as a non-conservative estimate, no surface correction is performed for Eq. (5.8b), thus providing an underestimation of the stress intensity factor. Additionally, the circular crack touches the pore surface only at a single point.

5.1.4. Crack instability. To determine crack instability, the local stress intensity factor is averaged over a virtual incremental crack surface ΔA [42]:

$$\overline{K} = \left[\frac{1}{\Delta A}\int K^2\, d(\Delta A)\right]^{1/2}. \tag{5.12}$$

This step has been introduced, since the stress intensity factor varies from point to point along the crack tip line, while propagation of the microcrack has to take place at least over the adjacent grain facets. For the semicircular crack model, it is assumed that the crack will propagate more likely along the pore surface where the stress concentration is maximized. This leads to the virtual crack geometry in Fig. 36a. Equation (5.13a) defines the averaged stress intensity factor, $\overline{K}$, based on Eqs. (5.8a) and (5.9) to (5.12):

$$\overline{K} = \left(\frac{4}{\pi}\int_0^{\frac{\pi}{2}} K_s^2\, \cos^2\varphi\, d\varphi\right)^{1/2}. \tag{5.13a}$$

For the circular crack model a different virtual crack geometry has to be chosen which fulfills the requirements of a non-conservative estimate. On the one hand, the geometry in Fig. 36b neglects the fact that the crack extends into the pore interior, but this is not relevant, since the the crack touches the pore surface only at a single

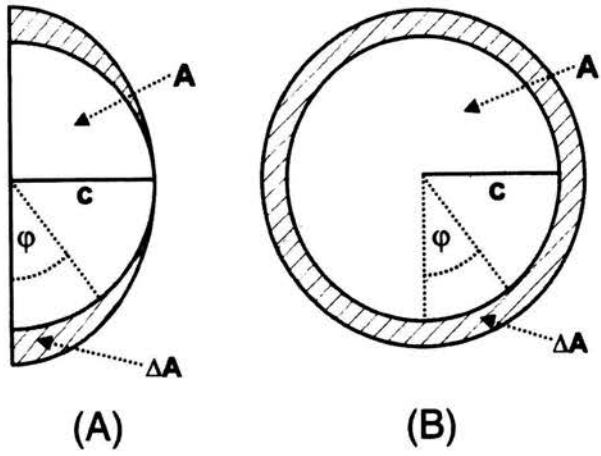

FIGURE 36. Virtual crack increments for: a) semicircular and b) circular crack crack.

point. On the other hand, there is a strong argument for the selection of the special geometry in Fig. 36b: it assigns the same weight to all sections of the crack tip line. Thus, the stress concentration due to the pore is in fact underestimated. The averaged stress intensity factor, $\overline{K}$, for the circular crack is calculated via Eqs. (5.8b) and (5.12):

$$\overline{K} = \left(\frac{1}{\pi} \int_{-\frac{\pi}{2}}^{\frac{\pi}{2}} K^2 \, d\varphi \right)^{1/2} . \tag{5.13b}$$

5.2. Results and discussion of the model

The normalized, local stress intensity factor, $K(\varphi)$, for a semicircular crack as defined by Eq. (5.8a) and a circular crack according to Eq. (5.8b) in the stress field of a pore is plotted in Figs. 37a and 6b as a function of relative crack length, c/R. As expected, the stress intensity factor reaches its maximum where crack tip line and pore surface are touching each other, i.e. at $\varphi = 0$ for the semicircular and at $\varphi = -\pi/2$ for the circular crack model. These points are relatively insensitive of the influence of relative crack length on the normalized stress intensity factor, because they are invariably surrounded by an area with high stress concentration. Therefore, the maximum of the local stress intensity factor is not a valuable fracture criterion, justifying the introduction of averaged stress intensity factors according to Eqs. (5.12) and (5.13). As shown in Fig. 37b, the normalized local stress intensity factor for angles other than $\varphi = -\pi/2$ approaches the value for an internal circular crack in an infinite medium ($2/\pi = 0.64$) at relative crack lengths, c/R, between 1 and 10. The averaged stress intensity factors as computed using Eqs. (5.13a) and (5.13b) are compared with the stress intensity factor of the circumferential crack according to Eqs. (5.1a) and (5.2) to (5.5) in Fig. 38. Again, it can be noticed that the

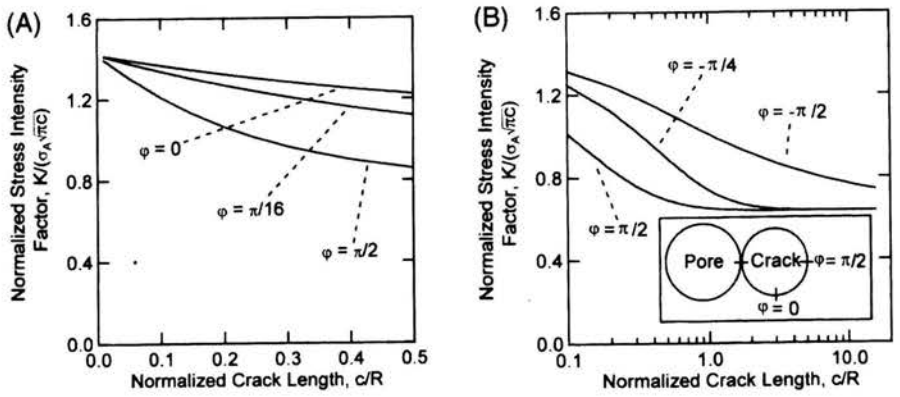

FIGURE 37. Normalized local stress intensity factor, $K/\sigma_A\sqrt{\pi c}$, for: (a) semicircular and (b) circular crack at the surface of a hemispherical pore as a function of relative crack length, c/R, for three different values of φ.

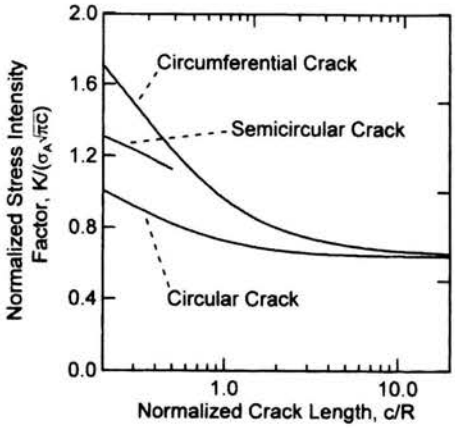

FIGURE 38. Normalized averaged stress intensity factor, $K/\sigma_A\sqrt{\pi c}$, for circular and semicircular cracks as compared to the normalized stress intensity factor for circumferential cracks at the surface of a hemispherical pore.

normalized, averaged stress intensity factor for the circular crack model as well as the normalized stress intensity factor for the circumferential crack approach the limit of $2/\pi$ at large crack lengths. These models form envelopes for the more realistic assumption of a semicircular crack.

It is the aim of this study to outline and interpret common trends observed in brittle fracture. Therefore, a normalized plot is developed which exhibits the characteristics of an Orowan-Petch plot, i.e. a plot of strength, σ_F, versus the inverse

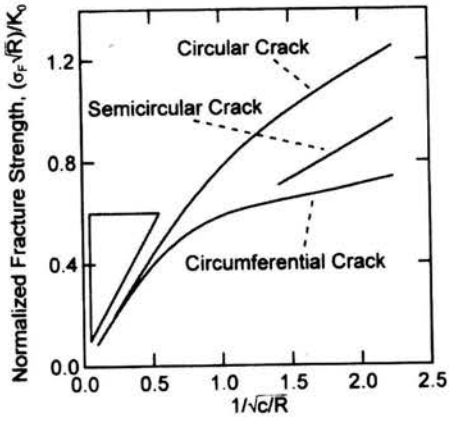

FIGURE 39. Generalized representation of the Orowan-Petch relationship between normalized fracture strength, $(\sigma_F\sqrt{R})/K_0$, and the inverse square root of the normalized crack length at instability, $1/\sqrt{c/R}$, for three defect configurations. The enclosed triangle provides visualization for the slope '1'.

square root of the average grain size, $\overline{G}$. As a link between microstructure and fracture mechanics, average grain size, $\overline{G}$, is substituted by the crack length, c. This is justified by the observation that the microcrack size is scaled with average grain size. At least as far as the Petch branch is concerned, the linear relationship between crack length at instability and average grain size is established [27]. The proportionality constant itself, however, depends on crack model and probably on material. In order to maintain a generalized description of the Orowan-Petch plot we therefore relate strength to crack size and a specific model and material will provide a specific conversion from microcrack size to grain size. For a given defect configuration, the strength, σ_F, is evaluated by equating the applied stress intensity factor, K_A, to crack tip toughness, K_0, and solving for σ_A. The influence of closure stresses is neglected as pointed out earlier, since closure stresses in many ceramics are small compared to strength. In order to treat brittle fracture in general, the strength, σ_F, is normalized by the crack tip toughness, K_0. The influence of a specific pore size is eliminated by multiplication of x- and y-axis with the square root of pore radius, R. Altogether, this procedure leads to a dimensionless plot of normalized strength, $y = (\sigma_F\sqrt{R})/K_0$, versus inverse square root of normalized defect size, $x = 1/\sqrt{(c/R)}$. Because this type of representation yields one universal curve for a given crack geometry, it is termed a generalized Orowan-Petch plot. In Fig. 39 this generalized representation is now applied to the three defect configurations described in the previous section.

In principle, the different models exhibit a division into two branches which is commonly observed in the Orowan-Petch plot:

1. The Orowan branch, i.e. the region of large grain sizes, can be fitted by a straight line with slope $1/y$, where the defect shape parameter y is defined in Eq. (5.14):

$$K_A = y\,\sigma_A\,\sqrt{c}. \tag{5.14}$$

   This line describes the typical behaviour of a Griffith flaw and reaches the origin for $c/R \to \infty$. For the limiting cases of a circumferential or a circular crack, respectively, the shape factor y obtains the value for a circular crack in an infinite medium, i.e. $2/\sqrt{\pi}$, while the applicability of the semicircular crack model is restricted to small, relative crack lengths as explained earlier. At $x = 0.5$, that is with the grain size being four times the pore size, circumferential crack and circular crack yield comparable results. For larger values of x, significant influences of the different stress concentration effects of the pore are noticeable with the circumferential crack yielding a 20% reduced strength at $R = c(x = 1)$ as compared to the circular crack.

2. In the Petch regime, i.e. the region of small grains, the slope decreases significantly due to the rising influence of local stress concentration for small relative crack lengths, c/R. As expected, the assumption of circumferential cracks as a conservative estimate leads to the flattest curve, while the circular crack model as the opposite envelope exhibits the largest increase with decreasing grain size. For the semicircular crack configuration as the most realistic description, an intermediate slope is observed. This behaviour is expected, because the crack tip line of a circular crack escapes the stress concentrating effect of the pore in average more than the semicircular crack and much more than the cir-

cumferential crack. As an approximation, the Petch branch may be described by a linear fit to the plotted curves in Fig. 39 with slope of 0.11, 0.31 and 0.34 for the circumferential, semicircular and circular crack model, respectively.
If a bilinear representation of the generalized Orowan-Petch plot is utilized, the transition point between Orowan and Petch regime is approximately located at $c/R = 1$. It can be concluded from Fig. 39, that it is insufficient to describe a strength versus grain size relationship only by means of grain size, since the size relation between the size of grains and stress concentrators is essential.
Let us first consider the case of constant pore size distribution and varied, average grain size. If a fine powder is sintered to full density, large pores keep a constant size [13, 43-45] during further heat treatment, while grain size still increases. Therefore it is expected that strength will decrease along a line close to the semicircular crack prediction in Fig. 39. This has, in fact, been verified experimentally for the Petch branch [27].

If samples are compared which were fabricated via different routes, i.e. with different size distributions of stress concentrators, then the size relationship between grain size and stress concentrator might vary from one sample to another. This explains why an experimental plot of strength versus the inverse square root of average grain size can never be described by a single line as in the case of the normalized Orowan-Petch plot, but is rather broadened into wide branches.

The conclusions drawn so far have been derived under the assumption of cracks originating at spherical pores being intersected by the sample surface. The physics of the problem, however, is unchanged if other stress concentrators like arbitrarily shaped pores or inclusions have to be considered. Transfer of our methodology to materials failing from other defects requires sound fractography and computation of the stress concentrating effect of the governing defect population (Eq. (5.1a,b)). The universal trend that a specific stress concentrator will produce instability loci is expected for any type of stress concentrator with both branches existing depending on the relative size of concentrator and crack.

5.3. Conclusions for the model

1. The influence of grain size on strength of ceramics as commonly described by the Orowan-Petch plot can be rationalized by describing fracture origins as combinations of a stress concentrator (in our case a large spherical pore) and a starter crack with length being governed by grain size.
2. In the Petch branch (grain size smaller than the stress concentrator) three different crack shapes were assumed and their stress intensity factors computed.
3. The two limiting crack configurations converge to one crack shape in the Orowan branch, where the grain size is larger than the stress concentrator.
4. The transition between both branches occurs at the point where the size of the stress concentrator equals the grain size.
5. The Orowan-Petch behaviour is not a fundamental function of grain size but rather a function of the ratio of grain size to size of the failure promoting stress concentrator.

6. A normalization procedure yields a generalized Orowan-Petch plot for brittle fracture independent of the size of microstructural features, crack tip toughness and strength.

6. Mechanical properties

Al_2O_3 with and without artificial pores was investigated with average grain size varying between $\overline{G} = 0.8\,\mu$m and $\overline{G} = 9.2\,\mu$m without significant change of morphology. Shrinkage of artificial pores during sintering obeys the linear law [43]:

$$d = d_0 \left[1 - \frac{1}{3\rho}(\rho - \rho_0)\right] \tag{6.1}$$

with d – the pore diameter, ρ – the density, and the subscript 0 denoting the presintered condition. Pore diameters measured by optical microscopy are in good agreement with predicted values (final pore size between 85 and 88 μm).

Fracture strength was obtained for four different grain sizes with and without large artificial pores with results seen in Fig. 40. The significant difference in strength for samples with and without artificial pores in combination with fractographic evidence verifies that fracture originates from the artificial pores. Therefore, in samples containing them, the artificial pore approach can be a powerful tool for relating fractographic and fracture mechanics studies.

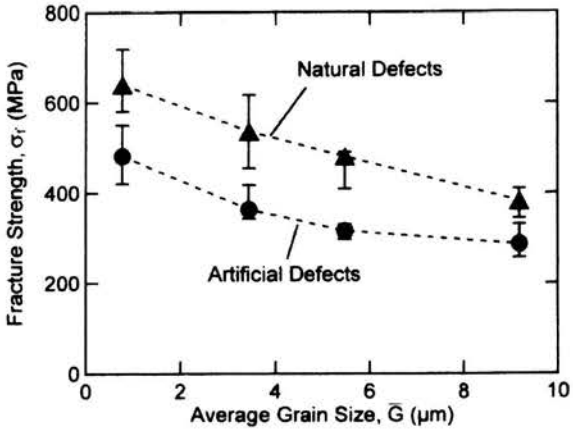

FIGURE 40. Strength as a function of grain size for material containing artificial spherical and natural defects.

Fracture origins for samples without artificial porosity could not clearly be identified. When artificial pores are present, strength decreases compared to samples without artificial flaws. The fracture surface shows at least one artificial pore at the tensile surface, which is split into two semispheres. Since the highest stress concentration is around the equator, these observations provide a strong hint that fracture

originates, with very few exceptions, from a single artificial pore which either intersects the tensile surface or which is at least located close to the surface as shown in Fig. 41.

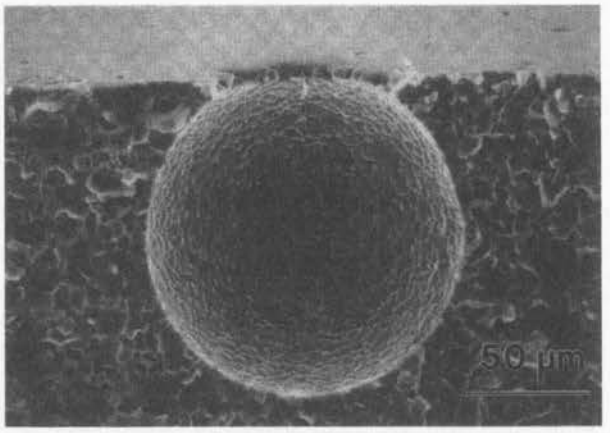

FIGURE 41. SEM micrograph showing partially embedded artificial spherical pore on the fracture surface in Al_2O_3.

The degree of embedding (measured from fractography) of these pores is plotted as a function of grain size in Fig. 42. While a very fine grained microstructure exhibits a narrow distribution of H/R with a mean value close to $H/R = 1$, a wide scatter of H/R can be observed for larger grain sizes. Fracture surfaces clearly demonstrate that fracture remains nearly completely intergranular as long as an equiaxed morphology can be maintained. Fractography of the sample group with

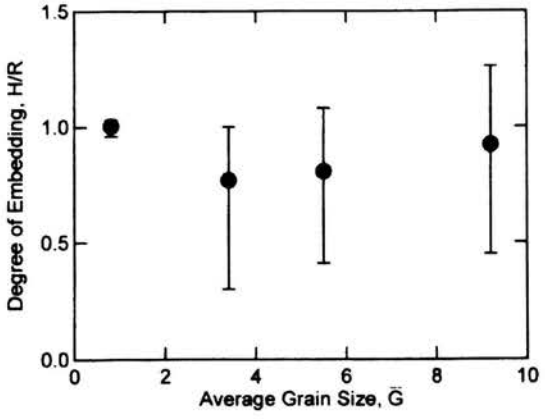

FIGURE 42. Degree of embedding, H/R, as a function of average grain size, $\overline{G}$, as measured on fracture surfaces.

$\overline{G} = 0.8\,\mu$m deserves special attention. Here, as shown in Fig. 43a, fracture tails can be clearly seen, as have also been observed in glass [16]. Particularly, this indicates failure from a localized defect in contradiction to the usual assumption of failure from a circumferential crack [17, 33, 34]. In Fig. 43b, one possible sequence of failure events which lead to the formation of fracture tails has been schematically shown. This feature could only be observed in the material with the smallest grain size, however, the larger roughness of the fracture surface in larger grained materials precluded clear identification of fracture tails.

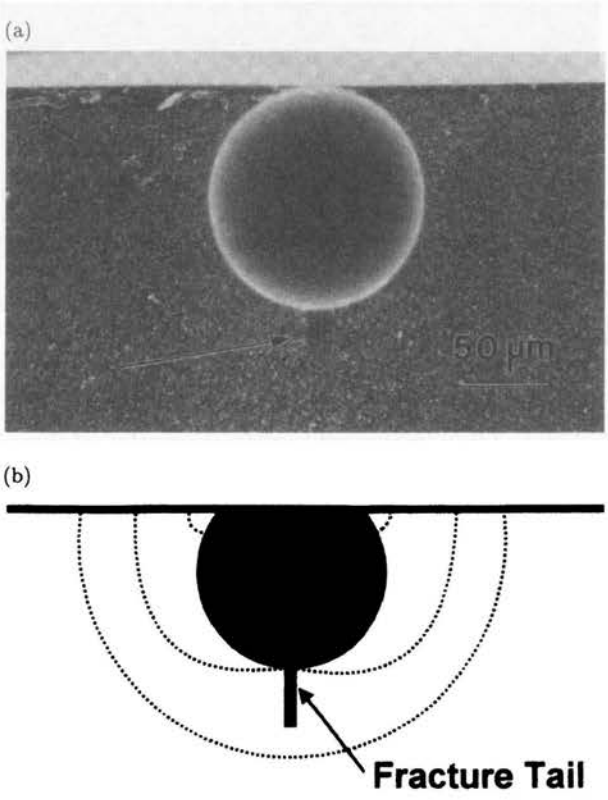

FIGURE 43. (a) Fracture tail as observed in the SEM, and (b) schematic diagram showing progression of crack fronts resulting in a fracture tail.

7. Discussion

A failure mechanism for alumina containing artificial spherical pores, which is applicable to analysis of the present strength data, has been proposed in another work [47]. Residual stresses resulting from thermal expansion mismatch exist throughout the body of the alumina [48]. These residual stresses, combined with an applied stress, cause microcracks of one facet length to be initiated. As resid-

ual stresses are caused by neighboring grains having different crystal orientations one facet length is of the order of one grain diameter. On applying stress, the first layer of grains around pores lies in the zone of highest stress concentration and is therefore a favorable location for this microcrack initiation. Microcracking releases the residual stresses. Therefore, the applied stress must be further increased until unstable growth of the initiated microcrack (or microcracks) occurs.

Confirmation of this series of events has been evidenced through the analysis of acoustic emissions obtained during fracture of alumina, containing artificial pores, loaded in 4-point bending [49]. Here acoustic emission signals were heard at 40-60% of the fracture stress during monotonic loading to fracture. These acoustic emissions could be ascertained to have originated within 1 mm of the fracture plane with acoustic emission activity much higher near the fracture plane than in other parts of the sample. They were therefore attributed to the formation of microcracks.

The present study, albeit not explicitly including residual stress effects, provides further evidence confirming the proposed fracture mechanism. Possible R-curve effects can now be analyzed more rigorously than before. As the full solution for the applied stress intensity factor for a semicircular crack (Eq. (11.2)) is now available, it can be compared with the crack resistance afforded by a 20 MPa constant closure stress setting at 10 μm grain size with pore diameter of 100 μm (Fig. 44). Figure 44 demonstrates that at equilibrium the increase in applied stress intensity factor with crack extension is much larger than the increase in fracture toughness, therefore leading to fracture without the occurence of stable crack growth. The R-curve in alumina has therefore no effect on fracture arising from a microcrack around a stress concentrator like a large pore.

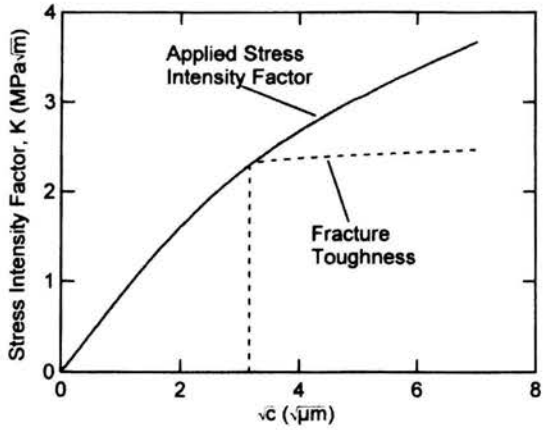

FIGURE 44. R-Curve as compared to the applied stress intensity factor around a pore (radius R = 50 μm) with a circumferential crack (constant closure stress of $p = 20$ MPa).

The present analysis has shown that fracture occurs from a microcrack at the surface of a spherical inclusion and not from a circumferential crack. Whereas our analysis was performed for the bottom of the surface pore, fracture tails in fine

grained alumina (Fig. 43) indicate that fracture may initiate more near the sample surface and are interpreted as two semicircular cracks joining at the pore surface. A more complete future analysis should, therefore, include the stress fields at other parts of the pore surface rather than just at the bottom, as considered in this work. Additionally, should the proposed failure mechanism be applicable and strength be limited by microcrack initiation, then the size of the critical microcrack at which fracture originates should scale with the microstructural facet length, i.e. the grain size.

Equation (5.10) can be inverted and solved for the critical crack size, c, with the result depicted in Fig. 45. The size of the critical microcrack, normalized with the average grain size is plotted as a function of grain size. Stress is taken to be the fracture stress of the sample under 4 point bending of the samples containing artificial pores. Fracture toughness is taken to be the crack-tip toughness of alumina, $2.3\,\mathrm{MPa}\sqrt{\mathrm{m}}$ [29], and is the governing material constant. It can be seen in Fig. 44 that for the samples with the three largest grain sizes, $\overline{G} \geqslant 3.4\,\mu\mathrm{m}$, that the critical microcrack size is in the region of twice the average grain size. Two points should now also be noted; firstly, that typical grain size distributions in MgO doped Al_2O_3 encompass grains on the order of twice the average grain size [50] and secondly, that residual stresses as a result of thermal expansion mismatch increase with grain size [48]. Hence a large grain, feasibly twice as large as an average grain, would be the most likely site for a critical microcrack to initiate. This result further confirms the proposed fracture model.

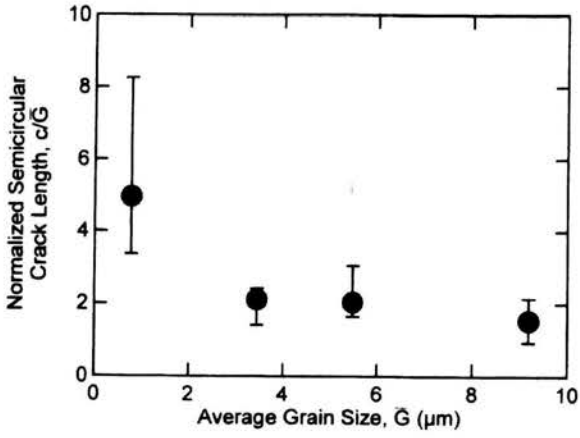

FIGURE 45. Critical crack length of semicircular flaws emanating from an artificial spherical pore normalized with the average grain size, $c/\overline{G}$, plotted against the average grain size, $\overline{G}$.

An exception is the material with an average grain size of $0.8\,\mu\mathrm{m}$. Here the reduced facet lengths and residual stresses should result in higher than obtained fracture stresses. Figure 45 shows a wide scatter in critical microcrack lengths for this material of 4-8 $\overline{G}$. A further anomaly is seen in Fig. 42 where the location of the

critical artificial pore in relation to the tensile surface of the bend bar is plotted. For $\overline{G} \geqslant 3.4\,\mu$m a wide range of pore locations is found ranging from partially embedded spherical segments to fully embedded partial spheres. In the case of the fine grain sized material, $\overline{G} = 0.8\,\mu$m, virtually all pores were embedded with the side just touching the tensile surface, $H/R = 1$. We believe that this is due to the interaction between the pore and the machining flaws for the smallest grain size materials as explained below.

It is proposed that for the larger grain sizes material is easily removed during machining at low levels of stress with grain boundaries providing the fracture path. Machining of samples with small grain sizes, on the other hand, requires much higher stresses to induce material removal due to microcrack inhibition. Under these circumstances surface damage entailing a small amount of breakout at the intersection of the pore and the tensile surface, for embedding ratio of $H/R = 1$, during machining is quite likely. This surface damage provides the initial microcracks for critical fracture, with the size of these microcracks not directly related to any microstructural feature like grain size.

For the finest grain sized material, therefore, a wide scatter in the size of fracture initiating microcracks combined with the dominance of the completely embedded sphere as the fracture origin induces the proposition that the strength is limited by pre-existing damage. For the larger grain sizes, however, the close scaling of critical microcrack size with average grain size and the wide scatter in the depth of the critical pores favors the assumption that strength is governed by microcrack initiation and subsequent instability. For these materials, with crack initiation limited fracture, strengthening may be obtained not only by increased short crack fracture toughness, but also by inhibition of microcrack initiation.

8. Conclusions

Existing models for fracture in brittle solids, originating from a spherical defect, were reviewed and extended. The applicability of the fracture mechanics analysis was investigated by determining the strength of alumina as a function of grain size with artificial, spherical pores. A complete approach was used to investigate the effect of grain size on the strength. This included generation of microstructure with controlled pores and grain size, experimental measurement of strength, fractography and fracture mechanics analysis of relevant failure origins. A number of conclusions can be drawn:

1. Spherical cavities act as stress concentrators and promote microcrack formation in the surrounding matrix.
2. R-curve behaviour in alumina is irrelevant for the strength, at least as far as the Petch-regime is concerned, only knowledge of the crack tip toughness of the material is required.
3. Analysis of a semicircular and circumferential crack located adjacent to a spherical pore are extended to include pore surface effects. Fracture occurs most probably from the semicircular crack configuration.
4. For larger grain sizes ($\overline{G} = 3.4$-$9.2\,\mu$m):

(a) the microcrack length depends on grain size. Thus, a microstructural parameter is introduced in a continuum mechanics background.

(b) the critical defect is created by interaction between processing defects, especially pores, and intrinsic defects, i.e. microcracks. This explains the moderate influence of grain size on strength in the Petch-regime.

5. At very small grain sizes ($\overline{G}$=0.8 μm) microcrack initiation is inhibited due to decreasing facet lengths and residual stresses. Strength is therefore limited by pre-existing machining damage.

II.B. Fracture of Alumina as a function of porosity

9. Introduction

The evolution of mechanical properties in ceramics and specifically alumina has been studied by several researchers in the case of free sintering. In particular, the influence of porosity on Young's modulus has been documented in detail in the literature [51-58]. A number of approaches have been developed to understand the evolution of strength as a function of porosity [59-64]. A phenomenological equation [59, 60] has been used to fit available data with porosities higher than about 60%. Recently, a description based on fracture mechanics was developed to model the evolution of strength by including the evolution of the size of the largest defect as well as the evolution of the crack tip toughness with densification [63]. In cases where the size of the largest defect varies by up to a factor of 5 [64] or the grain size varies by up to a factor of 10 [13, 14], a simple description based on a defect shape parameter is not sufficient and a defect has to be viewed as a combination of stress concentrator and incipient flaw.

Pressure-assisted sintering such as hot pressing is generally accepted to improve the microstructural homogeneity as well as the mechanical properties of ceramics. Much lower sintering temperatures and/or times are usually required to obtain the same density compared to free sintering. Thus grain growth can be reduced which in turn results in a more homogeneous microstructure and improved strengths. The accelerated densification during hot pressing of alumina is attributed to an increased sintering stress due to the externally applied pressure [65].

In assessing the possible effect, which an applied pressure can have on the evolution of mechanical properties during sintering, three issues require attention:

1. The influence of applied pressure on evolution of the largest defect by a long range creep mechanism.
2. The influence of applied pressure on rearrangement in the early stage of sintering.
3. The influence of applied pressure on the evolution of the contact area between particles and thereby the crack tip toughness of the material.

9.1. Influence of evolution of largest defect

According to Kingery and Francois [66], pores with a concave surface curvature are thermodynamically unstable and will shrink and finally disappear if kinetically

permitted. Pores with convex surface curvature, however, will shrink to an equilibrium size, dependent on grain size and dihedral angle. This equilibrium size is modified by an applied pressure [67]. Even with large applied pressures as occurring during hipping and sinter forging [67-70], the shrinkage of large pores may be kinetically hindered. The disappearance of either large artificial pores [67, 69, 70] or natural pores [69] in dense microstuctures was only achieved if the material exhibited sufficient plasticity [67] with a suffciently small grain size [67, 70] or contained a glassy phase [68]. A positive influence of hipping on the strength of alumina containing artificial pores [68] as well as zirconia toughened alumina containing natural defects [69] has been demonstrated. In contrast, nothing is known on the evolution of artificial or natural large defects during pressure assisted sintering. Without applied pressure, the evolution of the size of large artificial pores during densification has been studied by Flinn et al. [64]. They found that the shrinkage behaviour of the pores could be described by a simple shrinkage law in accordance to the macroscopic shrinkage of the sintering body.

9.2. Influence on rearrangement

Agglomerates may cause differential sintering and lead to fissures in the microstructures creating potential fracture origins. Conclusive observations of differential sintering and rearrangement, however, have only been demonstrated in two dimensions [71]. In a study on liquid phase sintering of alumina [63], the size of the largest flaw appeared not to be affected by rearrangement above the density of about 63%. On the other hand, rearrangement under an applied pressure may support densification by filling large voids by a buckling mechanism in powder arches [72]. A quantitative evaluation of rearrangement has not been reported yet, and its influence on the strength determining defect – with or without pressure – is unknown.

9.3. Influence on evolution of contact area

The effect of applied pressure on the evolution of crack tip toughness due to the evolution of contact area and thereby Young's modulus has not been studied. An increase in grain boundary diffusion coefficient or an increase in sintering pressure at fixed surface diffusion coefficient can lead to increased contact areas and non-equilibrium pore surfaces [73-75]. Equilibrium pore surfaces [76], however, appear to be maintained for a wide range of plausible ratios of surface diffusion coefficient and grain boundary diffusion coefficient [75, 77].

10. Mechanical properties of porous ceramics

Figure 46a shows the evolution of Young's modulus with the porosity for both hot pressing and free sintering. Each data point marks a single specimen. Included is the model given by Phani and Niyogi [53]:

$$E(P) = E_{100}\left(1 - \frac{P}{P_0}\right)^n, \tag{10.1}$$

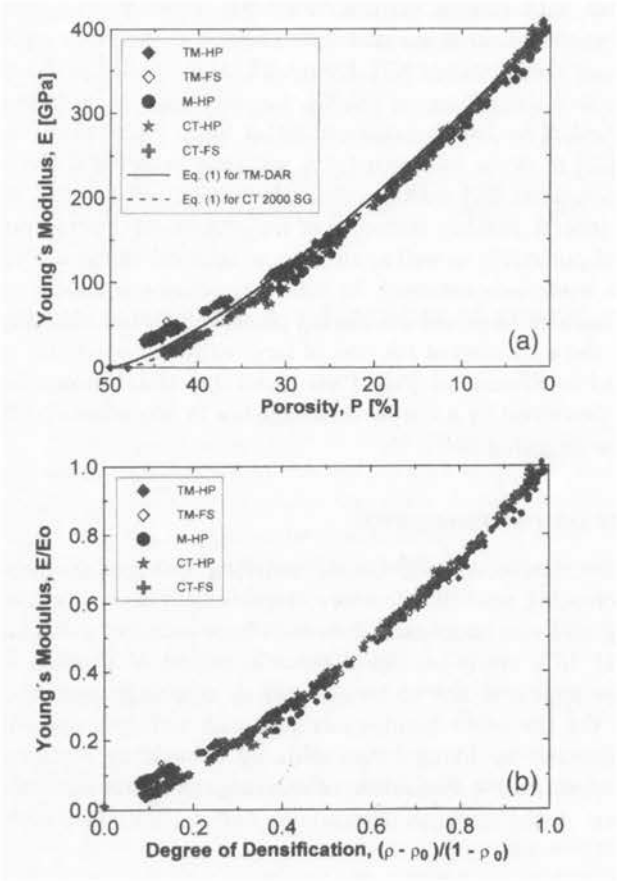

FIGURE 46. (a) Young's modulus vs porosity including the model given by Phani and Niyogi (Eq. (10.1)), and (b) normalized Young's modulus vs degree of densification, for hot-pressed and free sintered aluminas.

TABLE 3. Summary of the parameters $K_0(P=0)$, n, Y^2c_0 and P_0 for the powders TM-DAR and CT 2000 SG.

Powder	$K_0(P=0)$ [MPa$\sqrt{\text{m}}$]	n	Y^2c_0 [μm]	P_0 [%]
TM-DAR	2.0	1.35	19	50
CT 2000 SG	2.0	1.35	23	48

where $n = 1.35$ and $P_0 = 0.5$ (TM-series) and $n = 1.35$ and $P_0 = 0.48$ (CT-series), and $E_{100} = 404$ GPa (see Table 3 for a complete set of parameters used). The data of the two different processing routes clearly follow the same dependence upon the porosity. In the range $0 < P < 20\%$, the E-P-relationship is approximately linear.

Above $P = 20\%$, it deviates from linearity, and the slope decreases continuously with increasing porosity. In the initial stage of sintering, the samples made from both powders behave differently. The finer TM-DAR yields higher elastic moduli than the coarser CT 2000 SG. In order to eliminate density differences in the green body, Fig. 46b provides the normalized Young's modulus as a function of the degree of densification. The difference in elastic modulus in the initial stage is still visible. Note that there is no observable difference between the elastic moduli of the free sintered and hot pressed samples.

The dependencies of fracture toughness, K_{Ic}, and crack tip toughness, K_0, on porosity are shown in Fig. 47. $K_0(P)$ was calculated in the following manner: its maximum value $K_{0,\max}$ was obtained by measuring the near-tip crack opening displacement from the highest-density samples of HP and FS, and then K_0 was extrapolated to higher porosities by using a proportional relationship between K_0

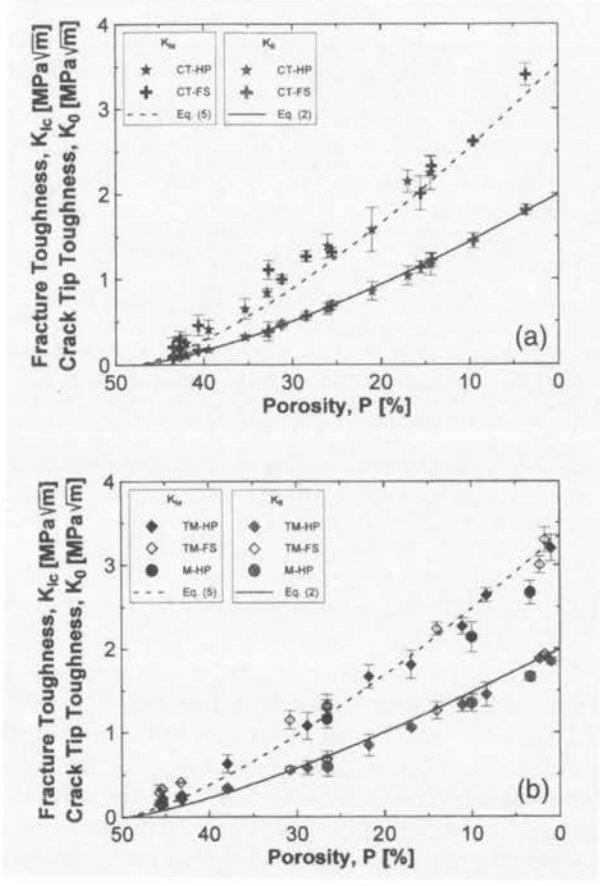

FIGURE 47. Crack tip toughness, K_0, and fracture toughness, K_{Ic}, as a function of porosity for hot-pressed and free sintered (a) CT samples, and (b) TM samples. Included is Eq. (10.2) (thick line) and Eq. (10.5) (dashed line).

and E [54, 55, 63, 64] (Eq. (10.2)):

$$K_0(P) = K_{0,100}\left(1 - \frac{P}{P_0}\right)^n. \tag{10.2}$$

Here $K_{0,100}$ is the crack tip toughness extrapolated to 100% theoretical density. K_0 measured from hot-pressed alumina was found to be equal to $1.9\,\mathrm{MPa}\sqrt{\mathrm{m}}$, for TM-DAR ($P = 1\%$) and $1.8\,\mathrm{MPa}\sqrt{\mathrm{m}}$, for CT 2000 SG ($P = 6\%$). In the case of free sintered samples, K_0 was equal to $2.0\,\mathrm{MPa}\sqrt{\mathrm{m}}$, for both TM-DAR ($P = 2\%$) and CT 2000 SG ($P = 4\%$). The measured values for the crack tip toughness show no influence of starting powder or processing conditions, as the accuracy of the method applied for indentation cracks is not better than $0.5\,\mathrm{MPa}\sqrt{\mathrm{m}}$ [29].

The energy absorbed at the crack tip, R_0, is taken to be related to the area fraction in analogy to the crack tip toughness (Eq. (10.2)), yielding Eq. (10.3), with $R_{0,100}$, the fracture energy of the fully dense alumina:

$$R_0(P) = R_{0,100}\left(1 - \frac{P}{P_0}\right)^n. \tag{10.3}$$

Accordingly, the energy absorbed in the crack wake by crack bridging, R_μ, depends on the number of effective bridging sites and is therefore assumed to be proportional to the contact area, providing Eq. (10.4), with $R_{\mu,100}$ the shielding term for the fully dense material:

$$R_\mu(P) = R_{\mu,100}\left(1 - \frac{P}{P_0}\right)^n. \tag{10.4}$$

A conversion from fracture energy to fracture toughness finally yields an equation for the fracture toughness of porous ceramics linked to the fracture toughness and the elastic modulus of the dense bodies (Eq. (10.5)):

$$\begin{aligned} K_{Ic}(P) &= \sqrt{\left(R_{0,100} + R_{\mu,100}\right) E_{100}\left(1 - \frac{P}{P_0}\right)^{2n}} \\ &= \left(1 - \frac{P}{P_0}\right)^n \sqrt{\left(R_{0,100} + R_{\mu,100}\right) E_{100}} = \left(1 - \frac{P}{P_0}\right)^n K_{Ic,100}. \end{aligned} \tag{10.5}$$

Equation (10.5) appears particularly appealing as the terms describing mechanical properties are separable from the terms describing porosity effects. In all stages, K_{Ic} is noticeably larger than K_0. The processing route has only negligible influence on both K_{Ic} as well as K_0. The suggested equations (Eq. (10.2) and Eq. (10.5)) describe the influence of porosity on both K_{Ic} and K_0 very well.

Figure 48 depicts the average fracture strengths as a function of porosity for both powders. In the range $P_0 > P > 25\%$, there is no detectable difference between hot pressing and free sintering. In the intermediate stage and final stage of sintering, the hot pressed samples reveal slightly higher strengths than the free sintered samples for the coarse-grained alumina. No difference is detected for the fine-grained powder. The modified hot pressing runs do not show differences compared with the

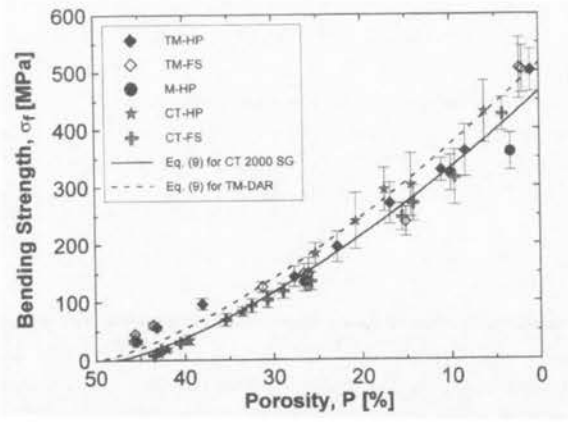

FIGURE 48. Fracture strength vs. porosity for hot-pressed and free sintered specimens. Included is Eq. (11.4) (thick line for coarse powder and dashed line for fine powder).

conventionally pressed specimens. The comparison of the two powders in the initial stage of sintering reveals a superiority of the fine-grained powder to the coarser material which is removed in the intermediate and final stages.

The results of the fractographic [79] analysis do not provide clear differences between hot pressed and free sintered samples and are therefore not reproduced here. As for failure causing flaws, pores, crack-like structures, porous and differentially sintered regions could be identified. In the highly porous samples, fracture marks were hardly detectable. Thus, a distinct fracture origin was not unequivocally visible.

11. Discussion

For hot pressing and free sintering, the experimental procedure chosen succeeded in producing samples with a wide variation in densities ranging from 55 to 99% TD. At the same sintering times, hot pressing yields slightly larger grain sizes as the densities are higher and pore drag is reduced. Significant grain growth only sets in at densities of 85 to 90% TD, close to the final stage sintering regime.

Hot pressing increases the densification rate. Thus, the pressure chosen (13 MPa) was sufficiently high to accelerate the driving force for sintering. According to Svoboda et al. [76], the hydrostatic sintering stress for alumina with the dihedral angle of 120°, the surface energy of $1\,J/m^2$ and the density of 70% with grain sizes of 0.2 and 1.0 μm can be computed to be 17.2 MPa and 3.5 MPa, respectively. The uniaxial pressure of 13 MPa therefore should have some effect on the densification of fine-grained powder, but a marked effect on the coarse-grained powder.

The following paragraphs are devoted to a discussion of the correlation of microstructural parameters and mechanical properties. The experimentally measured elastic moduli follow the same dependence on the porosity independently of the processing route (Fig. 46). In the initial stage, both sintering mechanisms lead to a

strong increase in Young's modulus with density as has been described by Green et al. for pressureless sintering [57, 58] and Ostrowski et al. for liquid-phase sintering [63]. This rapid increase has been attributed to fast neck growth. In this regime, a difference exists in the behaviour of the two powders. For the finer TM-DAR and at lower densities the Young's modulus increases much faster than for the coarser powder. This indicates that coarsening as compared to densification is more dominating in fine grained alumina as compared to coarse grained alumina in the initial stage.

The semi-empirical model given by Phani and Niyogi (Eq. (10.1)) provides a good data fit with the parameters n and P_0 as given in Part III. It is clear from those data that Eq. (10.1) cannot describe a non-densifying strong increase in Young's modulus in the early stages of sintering such as it can be seen in the case of TM-DAR. Conversly, this equation provides an appropriate fit for the CT powder. A previous study [47] successfully employed the same equation but with n being equal to 1.15 for liquid-phase sintered specimens. In the literature data can be found that imply an exponential dependence on porosity [52], or a purely linear E-P-relationship [62]. Our data are located somewhere in between. Fundamental relationships [76] based on an equilibrium pore surface area provide equations for the evolution of the contact area between grains, but require knowledge of the coordination number of particles as a function of density, which is not available.

Hot pressing does not affect the relationship of elastic modulus and porosity. This is in accordance with Riedel et al. for the late stage of sintering [77]. These predict, that if an applied hydrostatic stress is not greater than a few times the sintering stress, the shapes of intergranular pores as computed by Svoboda et al. (and thereby Young's modulus) are not altered and thereby the elastic modulus is not affected [76].

In the entire density range, $K_{Ic} > K_0$, reflecting R-curve behaviour even in porous alumina, consistent with related work on liquid phase sintered alumina [63]. Recently, Fett et al. [78] have shown that in alumina the crack closure forces due to bridging elements are very small (= 20 MPa). Stable crack growth emanating from processing-related flaws can therefore be neglected [13, 17]. For this reason, the strength is exclusively determined by the initial defect size and the crack tip toughness with $K_0(P)$ provided by Eq. (10.2).

Strength in porous ceramics with a shallow R-curve and concomitant negligible effect on strength can therefore be described using the Griffith criterion (Eq. (11.1)):

$$\sigma_f = \frac{K_0}{Y\sqrt{c}}, \tag{11.1}$$

and equations describing $K_0(P)$ and the defect size $c(P)$. Flinn et al. [64] suggested that shrinkage of large pores follows the macroscopic specimen shrinkage and demonstrated this dependence with measurements on artificial spherical defects. In our previous study on liquid phase sintered specimens [63], we have already utilized a similar dependence using engineering shrinkage strain [43] instead of true shrinkage strain [64]. This shrinkage law is provided by Eq. (11.2) with r the pore radius at the porosity P and r_0 the pore radius at the porosity P_0:

$$r(P) = r_0 \left(\frac{1 - P_0}{1 - P}\right)^{1/3}. \tag{11.2}$$

If great care is taken during surface machining and finishing, surface damage should play a minor role as a failure causing flaw, and processing related defects are the major fracture origins. The evolution of the defect shape parameter Y with decreasing porosity is not known. However, it can be assessed by using $K_0(P)$ in Eq. (10.2), $r(P)$ in Eq. (11.2), the Griffith relationship in Eq. (5.6) and the experimental results of the fracture strengths in Fig. 48. Rearranging Eq. (11.1) and for simplicity setting the crack size $c(P)$ as the size of the largest pore $r(P)$ yields:

$$Y^2 c(P) = \left(\frac{K_0(P)}{\sigma_f(P)} \right)^2 . \tag{11.3}$$

This approach was suggested by Flinn et al. [43] for artificially introduced flaws, and is applied here since we do not have any information about the evolution of the defect shape factor, Y, with the porosity yet. The equivalent flaw sizes are plotted in Fig. 49 for the CT and TM powders, respectively. Also included is Eq. (11.3) to describe the shrinking defect, assuming that Y remains constant. A least squares fit of both hot pressed and free sintered data sets yielded $Y^2 c_0$ of 19 μm for TM-DAR and 23 μm for CT 2000 SG.

For the fine-grained powder, the evolution of the equivalent flaw size with decreasing porosity follows the proposed shrinkage law very well. Pore shrinkage due to rearrangement has therefore no effect on the strength of the material except possibly for the first 5% of densification where no data could be obtained. For the coarse-grained powder, the shrinkage law also applies for $P < 40\%$. At $P > 40\%$ the high values of $Y^2 c$ can be due to either polishing damage [63] or may indeed be an indication of a rearrangement effect in the very early stages of sintering. As the large equivalent flaw sizes occur for both hot pressing and free sintering, polishing damage is considered the more likely cause for this effect. We therefore suggest that an essentially constant defect shape factor over a wide porosity range can be used to describe strength as a function of porosity. With large changes in grain size [13, 14], and pore size [64] more elaborate models specifying stress concentrators and starter defects need to be considered. As the change in grain size in our materials as well as size of the largest defect was small, we resort simply to combining Eq. (10.2), (11.2) and (11.3) and use $Y(P) = \text{const}$. The equation for the porosity dependent strength then reads [63]:

$$\sigma_f(P) = \frac{K_{0,100} \left(1 - \frac{P}{P_0}\right)^n}{\sqrt{Y^2 c_0 \left(\frac{1-P_0}{1-P}\right)^{1/3}}} . \tag{11.4}$$

This relation is plotted in Fig. 48. The parameters $K_0(P = 0)$, P_0, n and $Y^2 c_0$ are summarized in Table 3. The proposed equation is a good description of the experimental data for porosities smaller than 40%. In the initial stage, the model underestimates the measured data. The slight difference of Eq. (11.4) with Eq. (11.2) in our prior work on strength of liquid phase sintered alumina [63] is due to the use of engineering instead of true sintering strains in our older work.

The modified hot pressing runs had no positive effect on the defect size compared to the purely isothermal hot pressing cycle. A possible explanation may be that the

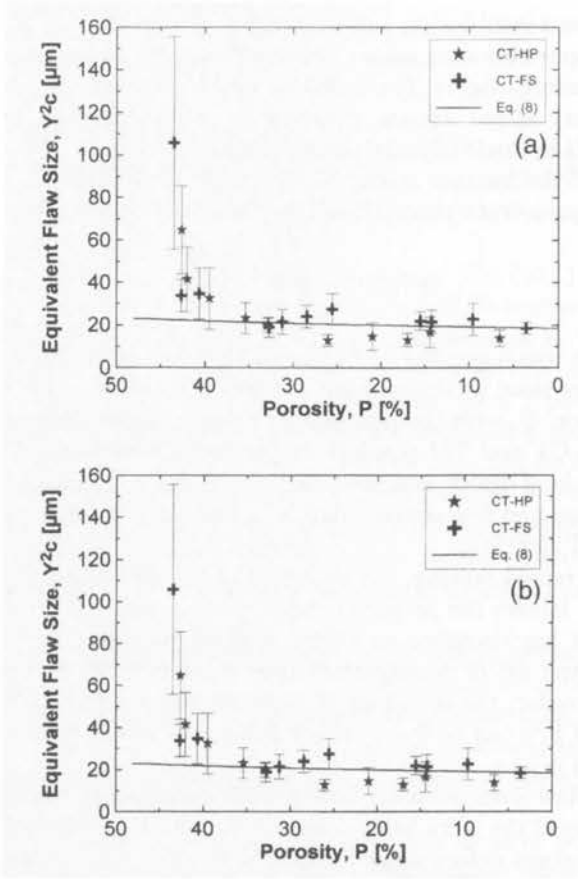

FIGURE 49. Equivalent flaw size vs. porosity for hot-pressed and free sintered samples: (a) CT powder, (b) TM powder. Included is also Eq. (11.3) (thick line).

viscosity at the onset of pressure is still too high. Thus, the microstructure is frozen rather than rearranged by the external pressure.

12. Conclusions

1. Strength of porous ceramics with small closure stresses can be described using a relation of crack tip toughness related to the evolution of Young's modulus with porosity, a shrinking defect in accordance with the macroscopic strain field and a constant defect shape factor.
2. An applied uniaxial pressure of 13 MPa had no mesureable influence on maintaining the equilibrium pore surface area as established for free sintering in both the aluminas used.
3. The applied pressure did not alter the evolution of defect size and defect shape factor for both our materials.

III. Graded and layered ceramics

13. Introduction

The concept of a compositional gradient within a material to attain specific functional properties has resulted in the development of functionally graded materials (FGM). This concept is not a new one, for example, case hardening of metals is a long-used process involving a microstructural and consequently hardness gradient. Recent research in this field has concentrated upon systems that involve stiffness and toughness gradients, which is usually a consequence of changes in other functional properties, e.g. refractoriness.

Ceramic coatings are usually considered brittle. However, a range of structural ceramics have enhanced toughness because interlocking grains bridge the crack in the region behind the crack tip leading to crack-growth resistance or R-curve behaviour [80-84]. Alternatively, by layering different structural ceramic materials the apparent fracture toughness can be increased through either enhancement of toughening mechanisms or residual stress effects [84-90]. Various processing techniques may also lead to a microstructural gradient within ceramic layers or coatings which is usually associated with a change in grain size and, hence presumably, a change in the crack growth resistance behaviour [91, 92].

Jin and Batra [93] calculated the R-curve behaviour of cracks extending parallel to the graded direction in a ceramic-metal FGM. The calculations showed that there was a "strong" R-curve behaviour when a crack grows from the ceramic rich region toward the metal-rich region. The results of the calculations were confirmed by experiments conducted on alumina/aluminum (ceramic/metal) gradient structure [94] where R-curves were measured for cracks extending parallel to the graded direction, from the ceramic rich to metal rich regions in the gradient. Additionally, several compositional profiles were considered which resulted in different crack growth resistance behaviour, demonstrating that the bridging by metallic ligaments of different graded volume fraction can affect the R-curve behaviour. A special weight-function analysis was used which accounted for the notable elasticity gradient in the sample [95]. However, for an elasticity difference across the graded region of $E_1/E_2 = 1.33$, the discrepancy in stress intensity factors that were calculated using a weight function which considered an elasticity gradient and one which did not was $< 10\%$ [94]. These works demonstrate that the effects of crack-growth resistance toughening by crack bridging, attributable to the compositional change, appear to have a far greater influence upon the crack growth behaviour than the resultant elasticity gradient.

A well recognized effect of producing composite materials with different thermal expansion behaviour is that residual stresses form within the composite. This is especially significant when high temperatures are used during processing. The measured fracture toughness and crack growth resistance behaviour, which depend on both microstructure and residual stress, become functions of position within composites having microstructural or macroscopic residual stress distributions [85-90, 93-96].

When measuring the R-curve behaviour of either multilayered or gradient composites, separating microstructure-related toughening mechanisms (i.e. crack bridg-

ing, kinking, transformation toughening, etc.) from residual stress-based mechanisms is difficult. It has already been demonstrated that the weight function analysis may be used to differentiate the influence of a macroscopic residual stress distribution (stepwise change in residual stress) from that of other microstructural mechanisms on the measured R-curve behaviour of a layered alumina-zirconia composite [89]. Experimental results showed that the macroscopic residual stress distribution significantly influenced the measured R-curve behaviour.

14. Experimental procedure and analysis

14.1. Sample preparation

Multi-layered alumina-zirconia composites were produced by sequential centrifugal consolidation [91, 92, 97, 98] of coagulated [91, 99] aqueous alumina-zirconia slurries. Further details of the centrifugal procedure used can be found elsewhere [103]. The composite green bodies were dried and then fired at 1600°C for 4 hr in air with 250°C/hr heating and cooling ramp rates. Two sintered discs were produced measuring 60 mm diameter by 10 mm thick and containing < 5% porosity.

Sintered discs were surface-ground flat using a 600 grit diamond wheel and multiple bend bars measuring 4 mm × 3 mm × 35 mm were then cut from the center of each disc. A V-notch was cut across the 3 mm × 35 mm face, perpendicular to the length of the bend bar as described in previous work [88, 101]. The V-notch radii, ρ, were measured to be 5 to 10 μm using optical microscopy. The 4 mm × 35 mm side-surfaces were additionally polished to 15 μm diamond abrasives to facilitate observation of crack growth.

Both monolithic (homogeneous) and graded specimens were produced (Table 4). The monolithic specimen, having a composition of 80 vol%-alumina-20 vol%-zirconia (80Al), was used to measure the R-curve behaviour without the influence of bulk thermal residual stresses or grain size variations. The graded specimens were pro-

TABLE 4. List of samples tested.

Sample	Layer Thickness [μm]	Testing Orientation	Sample Cross-Section [mm]		V-Notch Depth [μm]
			B	W	a_0
Monolithic	—	—	3.01	4.02	1050
1	~ 700	1	2.97	4.02	920
2	~ 700	1	2.96	4.03	935
3	~ 700	2	2.97	4.03	1045
4	~ 700	2	3.03	4.02	1340

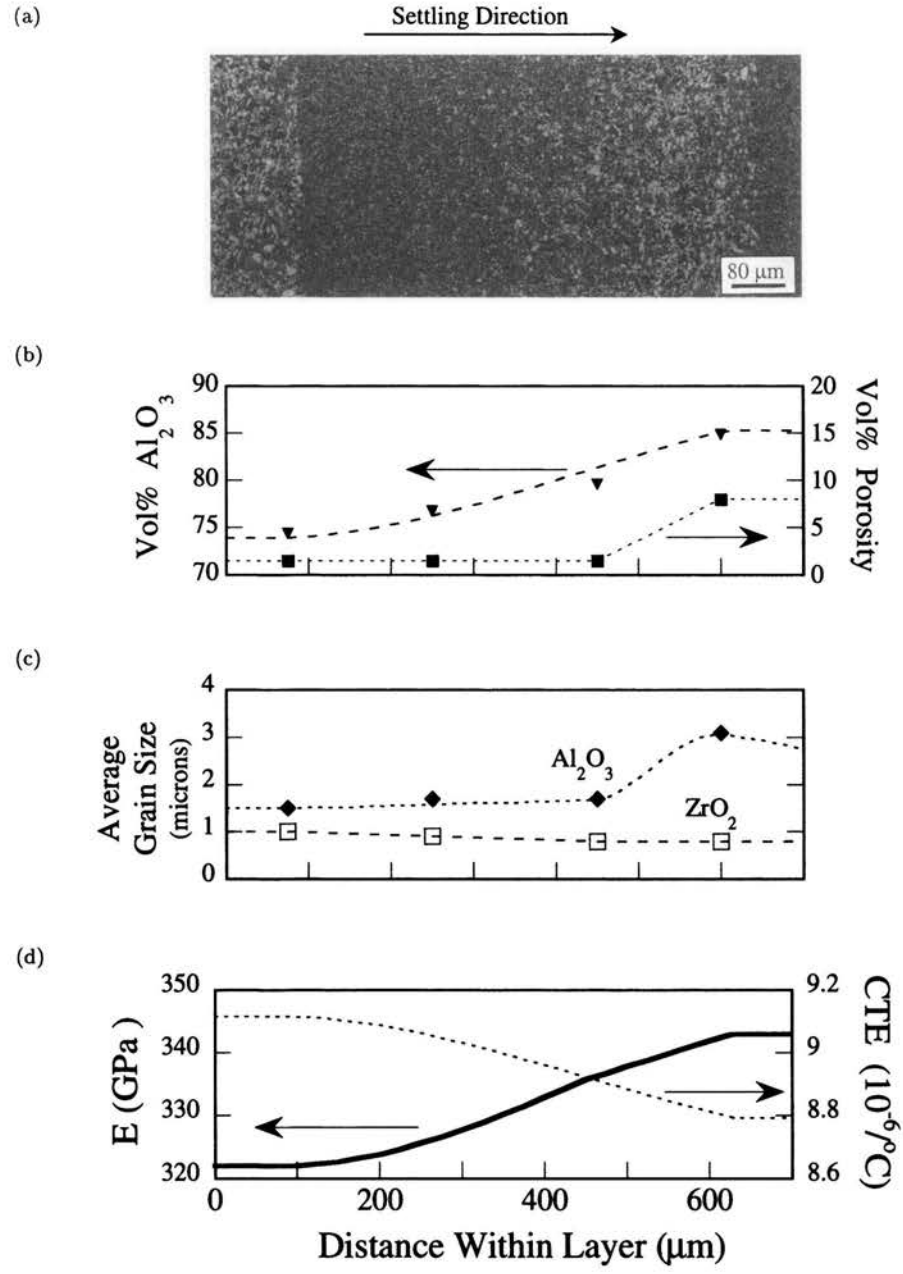

FIGURE 50. Orientation 1: The graded properties within each layer: a) optical micrograph, b) measured alumina vol% (▼) and porosity (■), c) the average grain size, and d) estimated Young's Modulus (—) and CTE (---). Note in (b) and (c) that the symbols mark measured data while the plotted curves are the estimated profiles used.

duced by centrifuging slurries having a solids composition of 76 vol% alumina[1] + 19 vol% zirconia[2] + 5 vol% platelike alumina[3]. During centrifugation, the larger platelike alumina particles (average particle diameter, $D_{50} = 9\,\mu m$) preferentially settled, producing a microstructural gradient as seen in Fig. 50a. The ASTM E562 standard point counting method (900 points per location) was used to determined the composition and porosity, while the ASTM E112-96e1 standard (duplex microstructure line intercept method) was used to estimate the average grain size. The results of these calculations are shown in Figs.50b and 50c, respectively. The Young's modulus, $E(x)$, Poisson's ratio, $\nu(x)$, and coefficient of thermal expansion (CTE), $\alpha(x)$, as a function of position within the layer were estimated by taking the geometric average of the upper (equal strains) and lower (equal stress) bounds of the Rule-of-Mixtures models using the material properties shown in Table 5. Figure 50d shows the results of this calculation for Young modulus and CTE across a single layer.

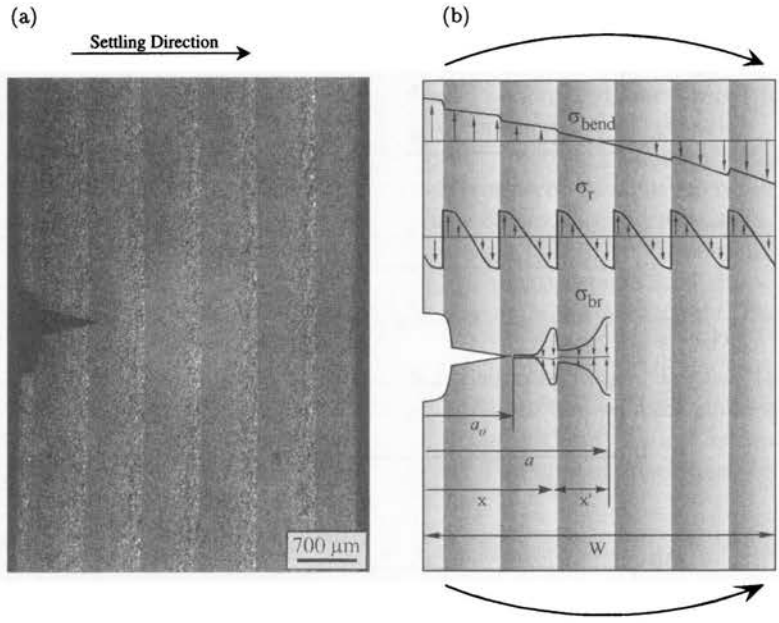

FIGURE 51. Orientation 1: a) Optical micrograph of the post cracked SEVNB sample showing the layer stacking with respect to the V-notch, b) A schematic of the three independent stress distributions acting within a specimen: bending ($\sigma_{bend}(x)$), residual ($\sigma_r(x)$), and bridging stress ($\sigma_{br}(x,a)$).

The graded samples tested in this investigation consisted of ~ 6 layers, a macrograph of a bend bar side surface is shown in Fig. 51a. The R-curve behaviour was tested in two different orientations with respect to the gradient within the layers.

[1] A16SG, 99.8%, $D_{50} = 0.4\,\mu m$, ALCOA, Bauxite, AR.
[2] CEZ-12, 98%, $D_{50} = 0.4\,\mu m$, American Vermiculite Corp., Marietta, GA.
[3] PWA 9, $D_{50} = 9\,\mu m$ Fujimi America Inc., Wilsonville, OR.

TABLE 5. Material properties of composite constituents.

Material	E [μm]	ν	α [10^{-6}/°C]
Al_2O_3	380[a)]	0.25[b)]	8.39[a)]
t-ZrO_2	205[a)]	0.32[a)]	11.5[a)]

[a)] Ref. [116], [b)] Ref. [117].

In orientation 1 (samples 1 and 2), the cracks were extended in the particle settling direction, i.e. from small to large grain size, and in orientation 2 (samples 3 and 4) the cracks were from large to small grain size.

14.2. Mechanical testing

Direct observations of crack initiation and extension were made on the bend bar side surfaces using a specialized four-point bend fixture placed on the stage of an optical microscope [88, 100, 102]. Loading was achieved using a piezoelectric translator and measured with a miniature load cell. A fluorescent dye penetrant (Met-L-Clek FP 90, Helling KG, GMBH, Hamburg, Germany) and an ultraviolet light source were used to measure crack lengths. The fluorescent dye was in contact with the V-notch tip during crack initiation and was within the crack during every subsequent crack extension. For slow crack extensions, the fluorescent dye immediately penetrated into the newly extended crack allowing crack extensions to be observed. There was no measurable influence of the fluorescent dye on crack extension [103].

Specimens were tested under displacement-control where subcritical crack initiation and further crack extensions ($\sim 10\,\mu$m increments) were achieved by loading at a slow rate. The incremental loading technique used is described elsewhere [88, 100]. The applied load to instigate crack propagation, P_c, and total flaw length, a, were measured and for each crack extension the apparent fracture toughness, K_R, was calculated as outlined below.

14.3. Weight function analysis

Bueckner [104] showed that the stress-intensity factor for an edge crack of depth a can be calculated by intergrating over the crack length the product of a weight function, $h(x,a)$, and any stress distribution $\sigma(x)$ acting normal to the fracture plane:

$$K = \int_0^a h(x,a)\,\sigma(x)\,dx, \tag{14.1}$$

where x is the distance along the crack measured from the surface. The weight function used must be derived for a specific crack-component configuration.

In the work of Fett and Munz [105-107] a weight function for an SENB sample and notch geometry is given by:

$$h(x,a) = \sqrt{\frac{2}{\pi a}} \frac{1}{\sqrt{1-\frac{x}{a}}\left(1-\frac{a}{W}\right)^{1.5}} \cdot \left[\left(1-\frac{a}{W}\right)^{1.5} + \sum A_{\nu\mu}\left(1-\frac{x}{a}\right)^{\nu+1}\left(\frac{a}{W}\right)^{\mu}\right], \quad (14.2)$$

where a is the total flaw length measured from the bend bar tensile surface and W is the sample width as shown in Fig. 50b. The values of the coefficients $A_{\nu\mu}$ and the exponents ν and μ are given in references [105] and [106].

14.4. Stress distribution

Three independent stress distributions were considered in this study: an applied bending stress distribution, residual thermal stress distribution, and a bridging stress distribution. The applied bending stress distribution for the monolithic sample, $\sigma^h_{\text{bend}}(x,P)$, was estimated using a standard bending-stress formula for homogeneous materials:

$$\sigma^h_{\text{bend}}(x,P) = \frac{1.5\,P(S_0-S_i)}{B\,W^2}\left(1-\frac{2x}{W}\right), \quad (14.3a)$$

where P is the applied load, S_0 and S_i are the outer and inner support spans of the four point bending fixture (in this study: 20 mm and 10 mm respectively), B is the sample thickness, and W is the sample height.

The applied bending stress distribution for the graded samples, $\sigma^g_{\text{bend}}(x,P)$, was estimated using a modified bending-stress formula in which the influence of the modulus variation across the bend bar cross-section is accounted for. The derivation is shown in the appendix. The resulting equation is specific to the sample geometry, the layer configuration, and elasticity gradient used in this investigation:

$$\sigma^g_{\text{bend}}(x) = \frac{P}{4B}(S_0-S_i)\,E'(x)\frac{E_2-E_1x}{E_2^2-E_1E_3}, \quad (14.3b)$$

where $E'(x)$ is the plane strain variation of modulus across the sample cross-section.

The residual thermal stress distribution within the graded composites, $\sigma_r(x)$, was estimated from the thermal expansion mismatch strains resulting from the variations of $E(x)$, $\nu(x)$, $\alpha(x)$ across the sample. The derivation is shown in the appendix.

$$\sigma_r(x) = \Delta T\,E'(x)\left[\alpha(x) + \frac{-A_1E_2^x + A_2E_1x + A_1E_3 - A_2E_2}{E_2^2-E_1E_3}\right]. \quad (14.4)$$

A $\Delta T = 1225°\text{C}$ was used for the temperature range over which the residual stress develops. When cooling from the sintering temperature to $\sim$ 1250°C, the thermal stresses developed within the sample were believed to be alleviated via creep [108, 109].

The bridging stress, σ_{br}, for the samples tested in the current study was believed to be caused by frictional pullout of interlocking grains, which resulted from the predominantly intergranular fracture mode [88, 89]. Phase transformation of the 15-25 vol% tetragonal zirconia was not detected along the fracture surface by X-ray diffraction [103], thus transformation toughening was assumed not to contribute to the bridging stresses.

The bridging stress distribution that acts along a given crack length will be dependent on the crack opening displacement (COD) along the crack length. For monolithic materials the bridging stress distribution, $\sigma_{br}(u)$, was taken to have an empirical power-law form similar to that which has been used previously [80-83, 110-112]:

$$\sigma_{br}^{h}(u) = \sigma_{max}\left(1 - \frac{u}{u^*}\right)^n, \tag{14.5}$$

where $2u$ is the COD, σ_{max} is the maximum stress supported by the bridging zone, n is a softening coefficient, and $2u^*$ is the critical COD in which closure stresses resulting from interlocking grains stop contributing to the bridging stress.

The weight function calculation used in this study required that the bridging stress function in Eq. (14.5) to be modified so that the bridging stress was a function of distance behind the crack tip rather then a function of COD. The COD was related to the distance behind the crack tip using the Irwin K-field plane-strain displacement relation, $u(x')$, developed for homogeneous materials:

$$\text{COD} = 2u(x') = 2\left[\left(\frac{8x'}{\pi}\right)^{\frac{1}{2}} \frac{K_0}{E/(1-\nu^2)}\right], \tag{14.6}$$

where x' is the distance behind the crack tip and K_0 is the intrinsic stress intensity factor that represents a lower bound for COD [83]. The COD estimate was simplified by using $K_0 = 3.6\,\text{MPa}\sqrt{\text{m}}$ and $E = 335\,\text{GPa}$, these values were based on the 80Al composition monolithic sample. Wake effects resulting from crack bridging will reduce the COD, however, due to the complexity of estimating these effects for graded materials, they were not considered.

Equation (14.5) was modified to be a function of distance behind the crack tip by substituting Eq. (14.6) in for both u and u^*: for the u substitution, x' was replaced with $a - x$, and for the u^* substitution, x' was replaced with L. The resulting equation relates the bridging stress as a function of distance behind the crack tip, $\sigma_{br}^{h}(x, a)$:

$$\sigma_{br}^{h}(x, a) = \sigma_{max}\left(1 - \frac{a-x}{L}\right)^n, \tag{14.7}$$

where $a - x$ is the distance from the crack tip and L is the steady-state bridging zone length, i.e. the critical distance behind the crack tip in which the COD is large enough so that closure stresses resulting from interlocking grains are zero, x^*. Values of $\sigma_{max} = 17\,\text{MPa}$, $n = 1$, and L=1000 μm were determined from experimentally measured data for a 80Al composition monolithic specimen, which has been described previously [89].

The bridging stress distribution acting along the crack will deviate from those estimated by Eqs. (14.5) and (14.7) due to the changing composition and grain size

as a function of location along the crack length, both of which may have an influence on the crack bridging capability of the material. The influence of the ~10 vol% Al_2O_3 compositional change across the graded region (Fig. 50b) on σ_{max}, n , and u_{cr} or L was believed to be minimal. This assumption was based on the observation that the initial R-curve (up to 300 μm) of the 90 vol%-alumina-10 vol%-zirconia (90Al) layered sample reported in reference [100] was accurately estimated with values of $\sigma_{max} = 17$ MPa, $n = 1$, and $L = 1000\,\mu$m calculated for the 80Al monolithic sample.

The influence of grain size on σ_{max} and n is unclear, thus were considered independent of grain size. Steinbrech et al. [82] showed that R-curves predicted with fixed σ_{max} and n values could accurately estimate the experimentally measured R-curve for alumina samples having 4, 9 or 16 μm grain sizes, suggesting that σ_{max} and n are not functions of grain size. However, Sohn et al. [111] have reported that n is dependent upon the grain size distribution within the material and in the analysis they considered that σ_{max} was also influenced by the grain size.

In this investigation the bridging stress distribution acting along the crack was believed to be dominated by the changing grain size, GS(x'), as a function of distance behind the crack tip. It is recognized that a large grain size requires greater CODs before separation of bridging grains occurs [82,112]. This critical COD* can be estimated if one considers that a single grain can only contribute to the bridging toughening mechanism if the COD at this given grain is less then one half the grain size, thus $2u^*(\mathrm{GS}) = \mathrm{GS}/2 = \mathrm{COD}^*$. For the case where the grain size changes with position along the crack the critical COD* that is necessary to end the bridging stresses for each x' location along the crack will be different. The bridging stress distribution as a function of grain size, $\sigma^g_{br}(\mathrm{GS}(x'))$, is given by:

$$\sigma^g_{br}(\mathrm{GS}(x')) = \sigma_{max}\left(1 - \frac{u(x')}{\frac{\mathrm{GS}(x')}{4}}\right)^n \tag{14.8}$$

where x' is the distance behind the crack tip. Equation (14.8) was modified to make it a function of distance behind the crack tip rather than a function of COD. Initially, Eq. (14.6) was set equal to GS/2, solved for x', where x' being the critical distance behind the crack tip in which complete grain separation occurs for a given grain size was renamed to, x^*:

$$x^* = \frac{\pi}{8}\left(\frac{E/(1-\nu^2)}{K_0}\,\frac{\mathrm{GS}}{4}\right)^2. \tag{14.9}$$

If the material had a homogeneous grain size this critical crack length would be the "steady-state" bridging zone length L. However, for composites with graded grain size regions there is no "steady-state" bridging zone length and Eq. (14.9) becomes a function of distance behind the crack tip, $x^*(x')$. For each location along the crack length the local grain size, GS(x), influences the size of the bridging stress that will be applied at that location. Substituting $x^*(x')$ into Eq. (14.7) for L and replacing x' with $a - x$ the resulting equation calculates the bridging stress as a function of distance behind the crack tip:

$$\sigma^g_{br}(\mathrm{GS}(a-x)) = \sigma^g_{br}(x,a) = \sigma_{max}\left(1 - \frac{a-x}{x^*(a-x)}\right)^n. \tag{14.10}$$

Figure 51b shows the distribution of these three stress contributions, σ^g_{bend}, σ_r and σ^g_{br}, within a graded sample loaded according to orientation 1.

14.5. Measured stress intensities

The weight function analysis was used to calculate the apparent stress intensity factor, K_R, from experimental data: the critical applied load to further extend a crack, P_c, and the average total flaw length, $a = (a_A + a_B)/2$, measured on both sides (A and B) of the sample. a_A and a_B are the sum of the V-notch depth, a_0, and the crack length as measured on sides "A" and "B" of the bend bar.

For the monolithic sample a standard bending–stress formula, Eq. (14.3a), was substituted into Eq. (14.1) and for each P_c vs. a data obtained from the experiment, the apparent stress intensity factor, K_R, was calculated. The procedure for the gradient samples was much the same as for the monolithic sample but the modified bending-stress formula, Eq. (14.3b), was substituted into Eq. (14.1) to account for the influences of the changing modulus across the sample.

14.6. Stress intensity factors

The stress intensity factors associated with each stress distribution were independently defined using the weight function analysis. The applied stress intensity factor for a homogeneous material, $K^h_a(x, P)$, was calculated with Eq. (14.3a) substituted in Eq. (14.1), whereas for the graded samples, $K^g_a(x, P)$, was calculated with Eq. (14.3b) substituted in Eq. (14.1). The stress intensity factor resulting from the residual stress distribution acting along the total flaw length, $K_r(x)$, was calculated with Eq. (14.4) substituted in Eq. (14.1). Note that the range of integration was over 0 to a.

The stress intensity factor resulting from the bridging stress distribution acting along the crack length for the homogeneous sample, $K^h_{\text{br}}(x, a_0)$, was calculated with Eq. (14.7) substituted in Eq. (14.1), and for the graded samples the stress intensity factor, $K^g_{\text{br}}(x, a_0)$, was calculated with Eq. (14.10) substituted in Eq. (14.1). Bridging stresses are considered to only act along the extended crack length, i.e. the region defined by $a_0 < x < a$, and thus the range of integration was over a_0 to a.

14.7. Stress intensity calculations

It is of particular interest to ascertain the effects of microstructural stresses due to crack bridging and residual stress upon the ultimate applied stress intensity factor for crack propagation. To this end, the principle of superposition was used to sum K_a, K_r, and K_{br} resulting in the crack tip stress intensity factor, K_{tip}, which is shown below:

$$K_{\text{tip}} = K_a + K_r + K_{\text{br}}. \tag{14.11}$$

For estimating the stress intensity factor for crack propagation as a function of total flaw length, a, Eq. (14.11) was solved for K_a, which was relabeled to K_R. Note that K_{tip} was replaced by the crack tip toughness, K_0 ($K_{\text{tip}} = K_0$ for crack extension). The resulting equation is:

$$K_R(a, a_0) = K_0(a) - K_r(a) - K_{\text{br}}(a, a_0). \tag{14.12}$$

For the monolithic sample, $K_0(a)$ was estimated by extrapolating the measured R-curve to the y-axis (located at a_0), resulting in $K_0^{80Al} = 3.6\,\mathrm{MPa}\sqrt{\mathrm{m}}$. Since the monolithic sample has a continuous composition, K_0 remained constant for all values of a. The stress intensity obtained using this technique is believed to give a reasonable estimate for K_0 because the effects of crack tip shielding and bridging would be minimized.

In an attempt to account for the modulus variations in the graded samples, the crack tip toughness, $K_0(a)$, was estimated following a procedure introduced by Lakshminarayanan et al. [85]. First, $K_a(a)$ was set equal to K_0 for the corresponding composition within the specimen and the critical applied bending load necessary to cause crack extension, P_c, as a function of total flaw length, a, was calculated. The P_c vs a results, incorporating the influence of the modulus variations, were then used in a standard formula for the stress intensity for a SENB specimen [101, 113] to calculate the $K_0(a)$ profile.

The intrinsic fracture toughness in the graded samples was assumed to vary as a function of composition across the layer where for the alumina richer region (85Al), $K_0^{85Al} = 3.4\,\mathrm{MPa}\sqrt{\mathrm{m}}$ and at the alumina poor region (75Al), $K_0^{75Al} = 3.8\,\mathrm{MPa}\sqrt{\mathrm{m}}$. The estimated values were based on extrapolations of the 80Al and 90Al measured R-curves to the y-axis, in which the intrinsic fracture toughness values of $K_0^{80Al} = 3.6\,\mathrm{MPa}\sqrt{\mathrm{m}}$ and $K_0^{90Al} = 3.2\,\mathrm{MPa}\sqrt{\mathrm{m}}$ were obtained, respectively [89, 100].

The $K_r(a)$ and $K_{\mathrm{br}}(a, a_0)$ profiles, being independent of the applied load, where simply calculated for several values of a.

15. Results

15.1. Bridging function

The bridging function for the graded samples was intended to account for the variation in crack growth resistance behaviour resulting from the grain size gradient within each layer. The bridging stress distribution that acts along a given crack length will depend on the difference between the COD along the crack length and the critical COD*. Figure 52a shows the COD profile for a homogenous material as a function of distance behind the crack tip (Eq. (14.7)), and superimposed on this plot is the critical COD* for a homogenous material with an average grain size of $1.9\,\mu\mathrm{m}$ (representative of the 80Al composition sample). Note that the crack tip is located at the far right of the figure. For distances behind the crack tip, where the critical COD* is greater than the COD of the crack, the grain size is large enough to bridge the crack and provide closure stresses. The example shown in Fig. 52a for the homogenous sample suggests that bridging stresses are acting along the crack until $\sim 900\,\mu\mathrm{m}$ behind the crack tip, and for further distances behind the crack tip, the COD of the crack is sufficiently large that grain bridging cannot occur.

The bridging stress distribution, as a function of distance behind the crack tip, for graded grain sized materials will be directly related to the variation of the critical COD* (Fig. 52b). The larger grain size in the platelike particle region of each layer results in a larger critical COD* and thus these regions can continue to contribute to the bridging stresses for much longer distances behind the crack tip (regions "b" in Fig. 52b).

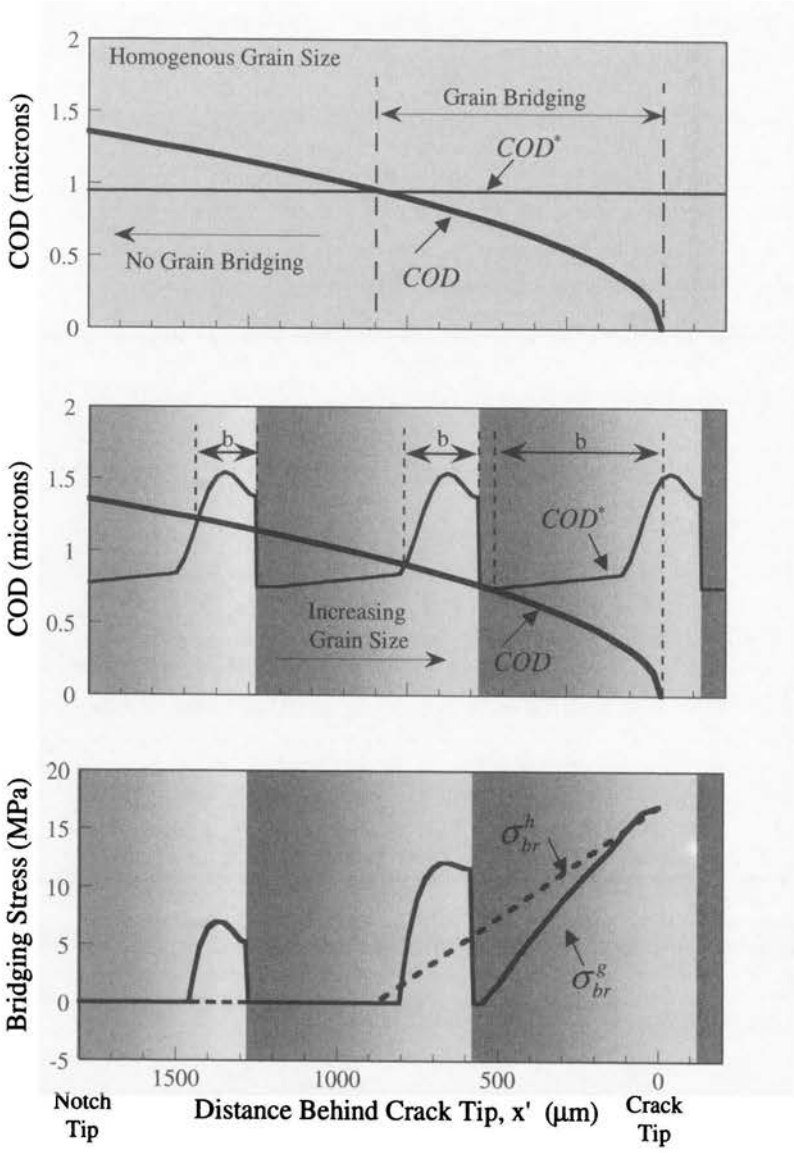

FIGURE 52. The location behind the crack tip in which the microstructure can bridge the crack and apply closure stresses (regions labeled "b") for: a) the homogeneous sample and b) the graded sample in orientation 1. c) The estimated bridging stress distribution acting along the 1800 μm crack length for the monolithic sample (- - -) and the gradient sample (—).

The bridging stress distribution, $\sigma_{\rm br}(x, a)$, resulting from the homogeneous and graded sample (sample 1) is shown in Fig. 52c. In this case the total flaw length was 2720 μm (920 μm notch depth + 1800 μm crack length), and the graph shows the bridging stress distribution acting along the crack as a function of distance

behind the crack tip. For the homogeneous sample the bridging stress distribution falls off linearly as a function of distance behind the crack tip and reduces to zero at $x' \approx 900\,\mu$m ($L = 900\,\mu$m in Eq. (14.7)). For the gradient sample the variation in the grain size significantly influenced the resulting stress distribution profile. Within the platelike particle regions the bridging stresses are still being applied at large distances behind the crack tip where the amount of bridging stress from the platelike particle regions decreases as the distance from the crack tip increases.

15.2. Calculated stress intensity profiles

Figures 53 and 54 show the calculated stress intensity profiles $K_0(a)$, $K_r(a)$ and $K_{\mathrm{br}}(a, a_0)$ for the graded specimens with a crack extending from the V-notch tip, length a_0, in orientation 1 and 2, respectively. With the sign convention used in

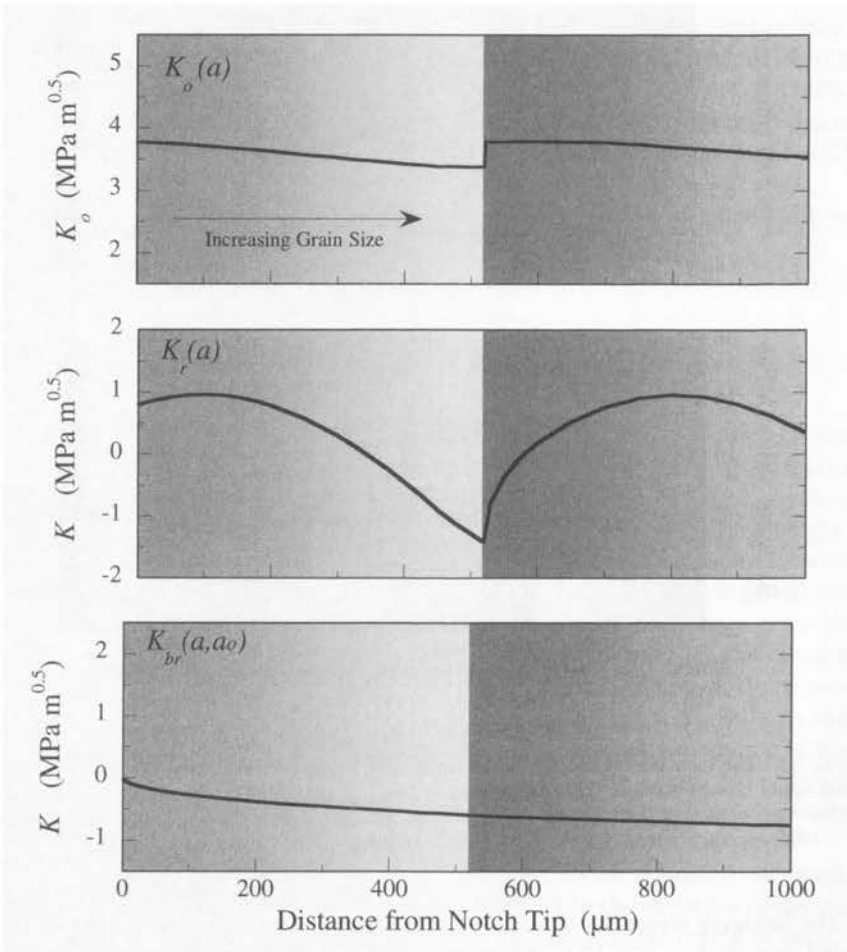

FIGURE 53. Orientation 1: A schematic of the estimated stress intensity factors as a function of position within the gradient specimen: a) K_0, b) K_r, c) K_{br}.

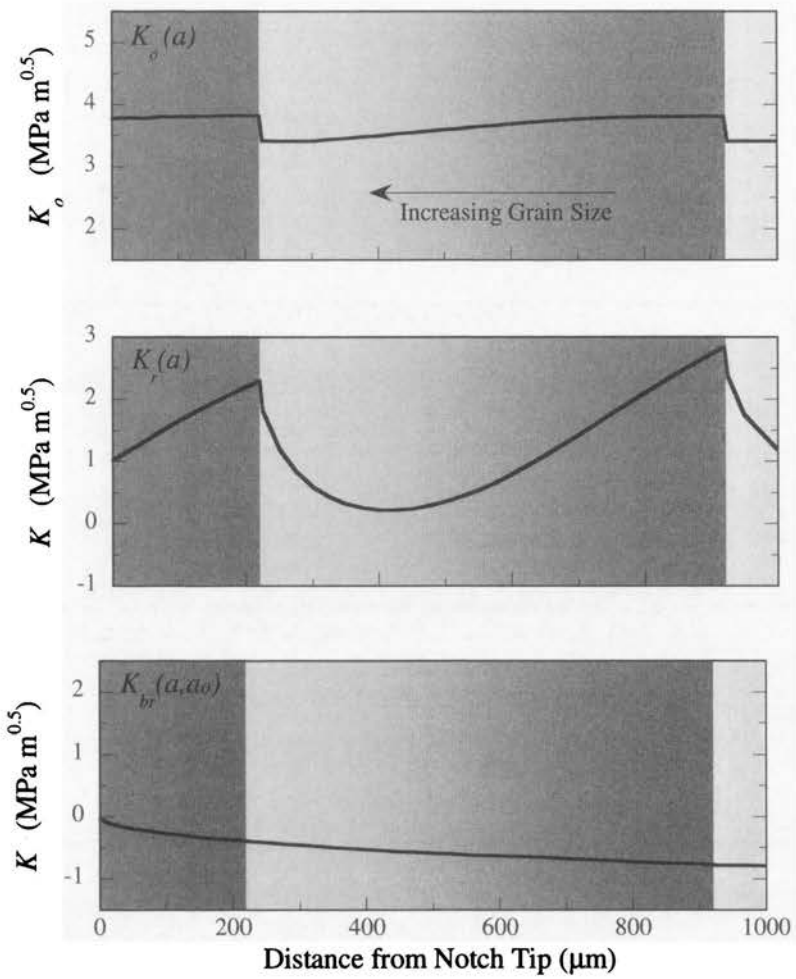

FIGURE 54. Orientation 2: A schematic of the estimated stress intensity factors as a function of position within the gradient specimen: a) K_0, b) K_r, c) K_{br}.

defining Eq. (14.11), $K_{\mathrm{br}}(a, a_0)$ acts to reduce the stress at the crack tip, where as for $K_r(a)$ the stress at the crack tip can be reduced or increased depending on the residual stress distribution. Additionally, the extent of influence of each component: $K_0(a)$, $K_r(a)$ and $K_{\mathrm{br}}(a, a_0)$ on the resulting $K_R(a, a_0)$ profile can also be seen.

15.3. Monolithic sample R-curve

The microstructure and R-curves for the monolithic sample are shown in Fig. 55. The plot consists of three curves: the measured R-curve, the calculated $K_R(a)$ profile and the estimated intrinsic crack tip toughness, K_0^{80Al}. The intrinsic crack

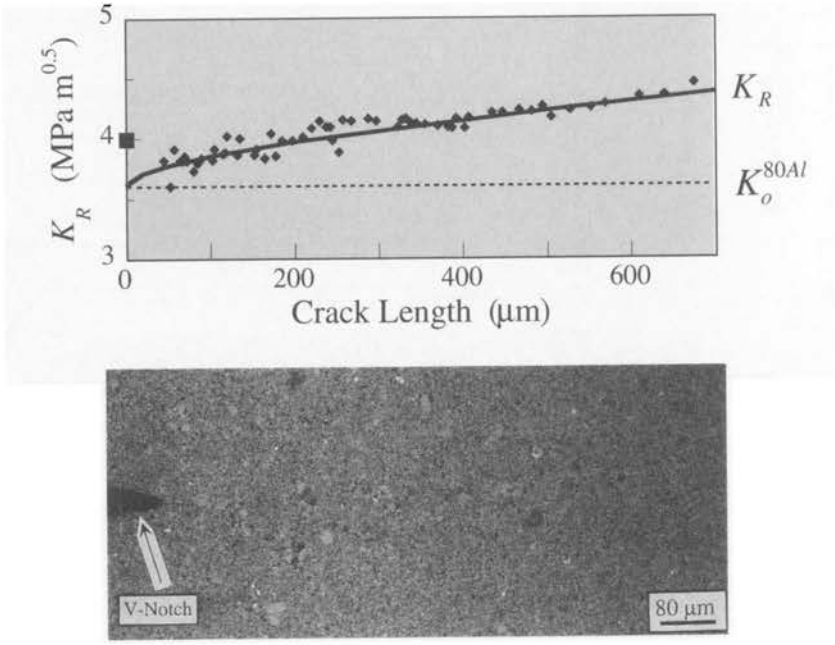

FIGURE 55. Monolithic specimen: a) The experimentally measured R-curve (♦) and the calculated $K_R(a, a_0)$ and K_0^{80Al} profiles. b) An optical micrograph of the post tested sample showing the microstructure that the crack propagated through. The ■ symbol on the K_R-axis represents the K_i for crack initiation from the V-notch tip.

tip toughness was estimated by extending the R-curve to the y-axis, resulting in $K_0^{80Al} = 3.6\,\mathrm{MPa}\sqrt{\mathrm{m}}$. The measured stress intensity for crack initiation from the V-notch, K_i was $4.0\,\mathrm{MPa}\sqrt{\mathrm{m}}$, in which the discrepancy between K_i and K_0^{80Al} was attributed to the shielding resulting from the relatively blunt ($\rho = 5\,\mu\mathrm{m}$) starter notch. The R-curve had a shallow rise where a $0.7\,\mathrm{MPa}\sqrt{\mathrm{m}}$ increase in K_R occurred after a $\sim 700\,\mu\mathrm{m}$ crack extension. The calculated $K_R(a, a_0)$ profile, using the Eq. (14.7) bridging stress distribution, estimated the R-curve behaviour of the 80Al material.

15.4. Graded sample R-curve

The microstructure and R-curves for the graded samples tested in orientation 1 (samples 1 and 2) and in orientation 2 (samples 3 and 4) are shown in Figs. 56 and 57, respectively. The plots consist of three curves: two measured R-curves and the calculated $K_R(a, a_0)$ profile for the given testing orientation. The similarity of the two measured R-curves for each testing orientation demonstrates the consistency of the R-curve measurement technique, while the proposed model describes the general R-curve behaviour of both sample configurations.

The direct superposition of several R-curves measured from layered or graded samples can be inappropriate due to the influences of starting the R-curve mea-

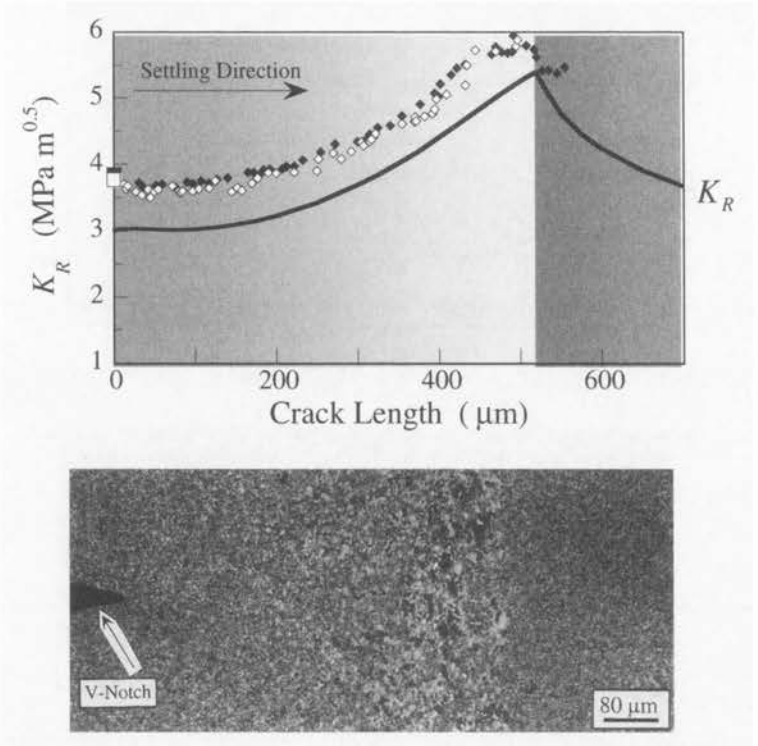

FIGURE 56. Orientation 1: a) The experimentally measured sample 1 (◇) and 2 (◆) R-curves and the calculated $K_R(a, a_0)$ profile. b) A representative microstructure through which the crack extended. The (□ and ■) symbols on the K_R-axis represent the K_i for crack initiation from the V-notch tip.

surement at different locations within the microstructure. For samples 1 and 2 the V-notch position (R-curve starting position) within a given layer were nearly identical, whereas the sample 4 V-notch was $\sim 20\,\mu$m closer to the bottom of the next layer as compared to sample 3. This problem was partially alleviated by lining up the layer interface for both samples through subtracting $20\,\mu$m from the measured crack length for each data point of the sample 4 R-curve.

The gradient microstructure resulted in an asymmetry in the measured R-curves and in the calculated $K_R(a, a_0)$ profile for orientations 1 and 2. The orientation 1 R-curves have a gradual increase in slope until the end of the platelike particle region was reached, resulting from the gradual increase in residual compressive stress and bridging stresses within the platelike particle region of the layer. The orientation 2 R-curves initially have a near flat R-curve until the crack impinged on the bottom of the next layer, the resulting steeper rise in K_R was due to the immediate increase in the residual compressive stress and bridging stresses.

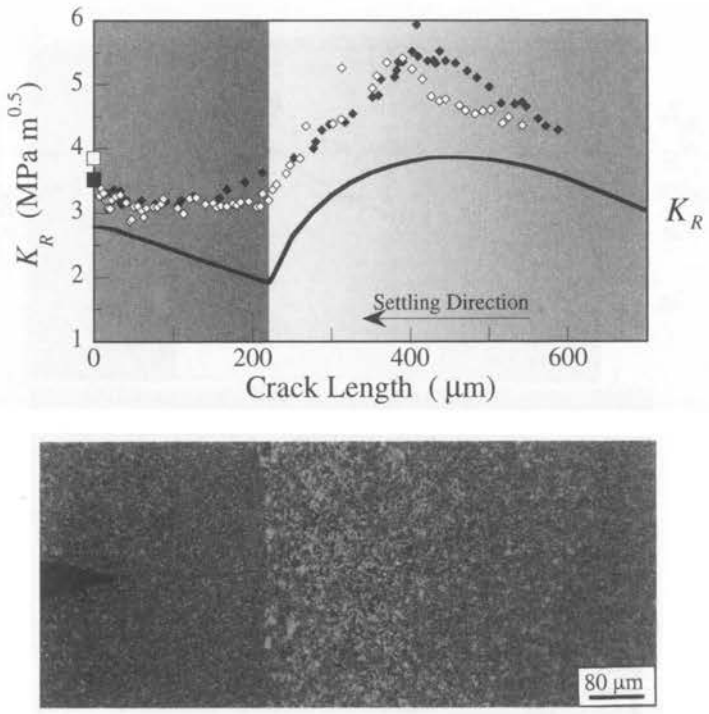

FIGURE 57. Orientation 2: a) The experimentally measured sample 3 (◊) and 4 (♦) R-curves and the calculated $K_R(a, a_0)$ profile. b) A representative microstructure through which the crack extended. The (□ and ■) symbols on the K_R-axis represent the K_i for crack initiation from the V-notch tip.

16. Discussion

16.1. Stress intensity calculation errors

Using a weight function, $h(x, a)$, that was developed for elastically homogenous samples for calculating the stress intensities for elastically graded materials, will result in errors. However, the extent of theses errors in the graded samples investigated in this study is believed to be less than 10%.

The studies by Erdogan [114] and by Jin and Batra [93, 115], demonstrate that the size of the elasticity change significantly influences the size of the deviation between stress intensity calculations that account for the elasticity variations and the ones that do not. For changes in modulus of $E_1/E_2 = 1.36$ across the graded region Jin and Batra [93] have shown that the deviation between stress intensity calculations that account for the elasticity variations and the ones that do not to be $\sim 10\%$.

The weight function that was used in this investigation was developed by Fett and Munz [105-107], and they have recently investigated methods for incorporating the influences of elasticity variations using a specialized weight function analysis [95].

They report that the procedures using the weight function analysis for graded materials were found not to change as compared to that for homogeneous materials [95]. The study by Chung et al. [94], using the weight function analysis developed by Fett and Munz, demonstrated that for a modulus variation of $E_1/E_2 = 1.33$ across the graded region that the difference in the calculated stress intensities between the homogeneous weight function analysis and the elastic graded weight function analysis was less than 10%.

The use of Eq. (14.1) may still not be entirely appropriate for calculating the stress intensities for the samples tested in this study in which the modulus change was $E_1/E_2 = 1.06$, however, for errors of $< 10\%$ this is considered reasonable.

16.2. Residual stress influence

By comparing the calculated stress intensity profiles: $K_0(a)$, $K_r(a)$ and $K_{\mathrm{br}}(a, a_0)$, shown in Figs. 53 and 54, it can be seen how each add up to obtain the final $K_R(a, a_0)$ profiles shown in Figs. 56 and 57, respectively. The $K_0(a)$ stress intensity provides the basis of the $K_R(a, a_0)$ profile. For the graded samples tested in this study, the $K_0(a)$ stress intensity variation across the graded region was only $\Delta = 0.4\,\mathrm{MPa}\sqrt{\mathrm{m}}$, the $K_r(a)$ variation was $\Delta = 2.7\,\mathrm{MPa}\sqrt{\mathrm{m}}$, and for $K_{\mathrm{br}}(a, a_0)$ the variation was $\Delta = 0.7\,\mathrm{MPa}\sqrt{\mathrm{m}}$ after $700\,\mu\mathrm{m}$ crack extension. This suggests that the variation in $K_r(a)$ will dominate the variation of $K_R(a, a_0)$ across the graded region.

It should be noted that for orientation 1 the $K_R(a, a_0)$ profile underestimated the measured R-curve by $\sim 0.75\,\mathrm{MPa}\sqrt{\mathrm{m}}$ over short crack lengths. This is unexpected since toughening by bridging is small at short crack lengths. For distances $< 10\,\mu\mathrm{m}$ from the notch tip both curves should have similar K_R values (Fig. 56). This difference was also apparent in samples 3 and 4, which were tested in orientation 2. Incorrect estimates of the elastic modulus and coefficient of thermal expansion across each layer may account for these deviations.

16.3. Bridging stress influence

The resulting bridging stress distribution shown in Figs. 53 and 54 demonstrated that the bridging stress relation derived for the gradient materials, Eq. (14.10), could be used to estimate the variable stress distribution associated with a changing grain size and with the distance behind the crack tip. This suggests if $\sigma_{\max}(x)$, $n(x)$ and $x_{\mathrm{cr}}(a - x)$ are estimated well, for a particular gradient, that a reasonable estimate of the bridging stress distribution acting along the crack can be calculated and the resulting K_{br} profile will describe the bridging toughening component.

In the current study, the bridging stress distribution between the monolithic sample and the graded samples were significantly different; however, the resulting K_{br} profiles were essentially the same. The bridging stress distribution for the graded samples was not significant enough to account for the discrepancies between the measured R-curve and the calculated $K_R(a, a_0)$ profile. It is possible that $\sigma_{\max}(x)$ and $n(x)$ may also vary as a function of position within the gradient, thus significantly altering the bridging stress distribution. Additionally, it should be noted that the estimated average grain size for the large grain sized regions of the graded layers ($\sim 3.1\,\mu\mathrm{m}$) is oversimplified, in which some of the platelike alumina grains

were nearly 10 μm long, suggesting that the COD* and $x^*(a-x)$ would actually be larger than the estimates used. However, the changes of $\sigma^g_{\mathrm{br}}(\mathrm{GS}(x'))$ resulting from this would not account for all the differences between the measured R-curve and the calculated $K_R(a, a_0)$ profiles.

17. Conclusions

1. The addition of a layered microstructure having a grain size and composition gradient within each layer was found to significantly alter the R-curve behaviour of alumina-zirconia composites. Additionally, the measured R-curve was influenced by the direction of crack extension with respect to the layered microstructure.
2. The weight function analysis demonstrated that the macroscopic residual stress distribution acting within a specimen can have a significant influence on the measured R-curve behaviour.
3. A bridging function used for monolithic materials was modified to account for the bridging stress variation as a function of a changing grain size as the crack extended through a graded microstructure. The influence of a variable grain size on the bridging stress distribution acting along a crack was demonstrated.

Acknowledgements

We gratefully acknowledge contributions by T. Ostrowski, A. Zimmermann, M. Hoffman, B.D. Flinn, R.K. Bordia, Tze-Jer Chuang, E.R. Fuller Jr., R.J. Moon, J. Hilden, K.J. Bowman and K.P. Trumble.

Appendix. Calculations for the bending and residual stress distributions across a repeating graded layered composite

The purpose of this appendix is to determine both bending stresses and residual thermal stresses as a function of position within each layer of a bend bar such as that shown in Fig. 58. Only normal stresses acting in the y-direction are treated. It is assumed that the variations in elastic modulus, Poisson's ratio, and thermal expansion coefficient are periodic (the same in each layer).

A.1. Bending stress distribution

This analysis estimates the bending stress distribution within graded samples tested in 4 pt bending. During testing it is assumed that the applied forces in the y-direction will be zero, and that the applied bending moment will be that for a

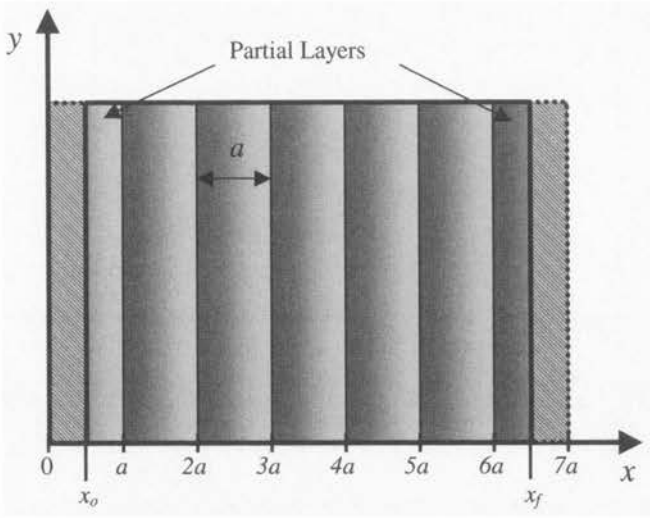

FIGURE 58. Schematic bend bar with graded layers. The tile contains five complete layers (thickness a) and two partial layers.

beam tested in 4 pt bending as shown below:

$$F = \int_{x_0}^{x_f} \varepsilon(x)\, E'(x)\, B\, dx = 0, \tag{A.1}$$

$$M = \int_{x_0}^{x_f} \varepsilon(x)\, E'(x)\, B\, x\, dx = \frac{P}{4B}(S_0 - S_i), \tag{A.2}$$

where $E'(x)$ is the elastic modulus corrected for plane strain, B is the sample thickness, P is the applied load, and S_0 and S_i are the outer and inner loading span lengths for 4 pt bending.

Due to variations in $E(x)$ across the sample the local strains were assumed to vary as:

$$\varepsilon(x) = a_b\, x + b_b, \tag{A.3}$$

where a_b and b_b are constants. By substituting Eq. (A.3) into Eqs.(A.1) and (A.2), the constants a_b and b_b are found:

$$a_b = -\frac{P}{4B}\,(S_0 - S_i)\,\frac{E_1}{E_2^2 - E_1\, E_3}, \tag{A.4}$$

$$b_b = \frac{P}{4B}\,(S_0 - S_i)\,\frac{E_2}{E_2^2 - E_1\, E_3}, \tag{A.5}$$

where

$$E_1 = \int_{x_0}^{x_f} E'(x)\,dx, \tag{A.6}$$

$$E_2 = \int_{x_0}^{x_f} x\,E'(x)\,dx, \tag{A.7}$$

$$E_3 = \int_{x_0}^{x_f} x^2\,E'(x)\,dx. \tag{A.8}$$

Substituting Eqs. (A.4) and (A.5) into Eq. (A.3) and using the relation $\sigma(x) = \varepsilon(x)\,E'(x)$, a final bending stress relation is obtained:

$$\sigma^g_{\text{bend}}(x) = \frac{P}{4B}\,(S_0 - S_i)\,E'(x)\left[\frac{E_2 - E_1\,x}{E_2^2 - E_1\,E_3}\right]. \tag{A.9}$$

A.2. Residual thermal stress distribution

Upon heating the tile in Fig. 58 to a temperature at which creep occurs readily, the tile will assume a condition of zero stress. If the tile is then cooled an amount, ΔT, but is constrained in the y-direction so that no thermal contraction occurs, then a net tensile stress will develop. The variations in CTE and elastic modulus within each layer will produce variations in the stress. The strain at any point is given by:

$$\varepsilon(x) = \varepsilon^{\text{th}}(x) + a_r\,x + b_r, \tag{A.10}$$

where $\varepsilon^{\text{th}}(x)$ is the thermal contraction, $(\alpha(x)\Delta T)$, $(a_r\,x + b_r)$ accounts for warping of the tile resulting from non-symmetric variations in $\alpha(x)$, across the sample, and a_r and b_r are constants. The values of a_r and b_r must be determined such that the net load and bending moment exerted by the tile are zero. The net load, F, and bending moment, M, are given by:

$$F = \int_{x_0}^{x_f} \varepsilon(x)\,E'(x)\,B\,dx = 0, \tag{A.11}$$

$$M = \int_{x_0}^{x_f} \varepsilon(x)\,E'(x)\,B\,x\,dx = 0. \tag{A.12}$$

Solving for a_r and b_r one obtains:

$$a_r = -\Delta T\left(\frac{A_1\,E_2 - A_2 E_1}{E_2^2 - E_1\,E_3}\right), \tag{A.13}$$

$$b_r = \frac{\Delta T\,A_1\,E_3 - \Delta T\,A_2\,E_2}{E_2^2 - E_1\,E_3}, \tag{A.14}$$

where E_1, E_2 and E_3 are defined by Eqs.(A.6), (A.7), and (A.8), respectively, and A_1 and A_2 are defined as follows:

$$A_1 = \int_{x_0}^{x_f} \alpha(x)\, E'(x)\, dx, \tag{A.15}$$

$$A_2 = \int_{x_0}^{x_f} x\, \alpha(x)\, E'(x)\, dx. \tag{A.16}$$

The residual thermal stress relation is obtained by substituting Eqs. (A.13) and (A.14) into Eq. (14.10) and using the relation $\sigma(x) = \varepsilon(x)\, E'(x)$. Finally, the final residual thermal stress relation is obtained:

$$\sigma_r(x) = \Delta T\, E'(x) \left[\alpha(x) + \frac{-A_1\, E_2\, x + A_2\, E_1\, x + A_1\, E_3 - A_2\, E_2}{E_2^2 - E_1\, E_3} \right]. \tag{A.17}$$

References

1. D. MUNZ and T. FETT, *Ceramics - Mechanical Properties, Failure Behaviour, Materials Selection*, Springer-Verlag Berlin, 1999.
2. J. RÖDEL, *Rissüberbrückung in keramischen Werkstoffen*, VDI-Verlag GmbH Düsseldorf, 1993.
3. A.G. EVANS and F.W. ZOK, The physics and mechanics of fibre-reinforced brittle matrix composites, *Journal of Materials Science*, Vol.29, pp.3857-3896, 1994.
4. H. PRIELIPP, M. KNECHTEL, N. CLAUSSEN, S.K. STREIFFER, H. MÜLLEJANS, M. RÜHLE and J. RÖDEL, Strength and fracture toughness of aluminium/alumina composites with interpenetrating networks, *Materials Science and Engineering*, Vol.A197, pp.19-30, 1995.
5. D.J. GREEN, R.H.J. HANNINK and M.V. SWAIN, *Transformation Toughening of Ceramics*, CRC Press Inc. Boca Raton, 1989.
6. A.B. SCHÄUFELE and K.H. HÄRDTL, Ferroelastic properties of lead zirconate titanate ceramics, *J. Am. Ceram. Soc.*, Vol.79, No.10, pp.2637-40, 1996.
7. S. LUCATO, D. LUPASCU and J. RÖDEL, Effect of poling direction on R-curve behaviour in PZT, *J. Am. Ceram. Soc.*, Vol.82, pp.424-426, 2000.
8. J. KOCH, *Piezoxide*, Valvo Philips Bauelemente, Dr. Alfred Hüthig Verlag GmbH, Heidelberg 1988.
9. R.C. GARVIE, R.H. HANNINK, and R.T. PASCOE, Ceramic steel?, *Nature*, Vol.258, pp.703-704, 1975.
10. R.M. MCMEEKING and A.G. EVANS, Mechanics of transformation-toughening in brittle materials, *J. Am. Ceram. Soc.*, Vol.65, pp.242-246, 1981.
11. I-WEI CHEN, Model of transformation toughening in brittle materials, *J. Am. Ceram. Soc.*, Vol.74, pp.2564-72, 1991.
12. R.H.J. HANNINK, P.M. KELLY and B.C. MUDDLE, Transformation toughening in zirconia-containig ceramics, *J. Am. Ceram. Soc.*, Vol.83, No.3, pp.461-87, 2000.
13. A. ZIMMERMANN, M. HOFFMAN, B.D. FLINN, R.K. BORDIA, T.-J. CHUANG, E.R. FULLER and J. RÖDEL, Fracture of alumina with controlled pores, *J. Am. Ceram. Soc.*, Vol.81, No.9, pp.2449-57, 1998.

14. A. ZIMMERMANN and J. RÖDEL, Generalized Orowan-Petch plot for brittle fracture, *J. Am. Ceram. Soc.*, Vol.81, No.10, pp.2527-32, 1998.

15. T. OSTROWSKI and J. RÖDEL, Evolution of mechanical properties of porous alumina during free sintering and hot pressing, *J. Am. Ceram. Soc.*, Vol.82, No.11, pp.3080-86, 1999.

16. R.W. RICE, Pores as fracture origins in ceramics, *J. Mat. Sci.*, Vol.19, pp.895-914, 1984.

17. J. SEIDEL, N. CLAUSSEN, and J. RÖDEL, Reliability of alumina ceramics, I: Effect of grain size, *J. Eur. Ceram. Soc.*, Vol.15, pp.395-404, 1995.

18. A.G. EVANS, A dimensional analysis of the grain-size dependence of strength, *J. Am. Ceram. Soc.*, Vol.63, No.1-2, pp.115-116, 1980.

19. R.W. RICE, Strength grain size effects in ceramics, *Proc. Brit. Ceram. Soc.*, Vol.20, pp.205-207, 1972.

20. R.W. RICE, Microstructure dependence of mechanical behaviour, *Treatise on Materials Science and Technology*, Vol.11, pp.199-381, R.K. MacCrone [ed.], 1977.

21. S.C. CARNIGLIA, Reexamination of experimental strength-vs.-grain-size data for ceramics, *J. Am. Ceram. Soc.*, Vol.55, pp.243-49, 1972.

22. N.M. ALFORD, K. KENDALL, W.J. CLEGG and J.D. BIRCHALL, Strength/microstructure relation in Al_2O_3 and TiO_2, *Advanced Ceramic Materials*, Vol.3, pp.113-17, 1988.

23. R.W. RICE, Ceramic tensile strength-grain size relations: grain sizes, slopes, and intersections, *J. Mat. Sci.*, [in press].

24. (a) P. CHANTIKUL, S.J. BENNISON and B.R. LAWN, Role of grain size in the strength and *R*-curve properties of alumina, *J. Am. Ceram. Soc.*, Vol.73, No.8, pp.2419-27, 1990.

    (b) R.W. RICE, Comment on "Role of grain size in the strength and *R*-curve properties of alumina", *J. Am. Ceram. Soc.*, Vol.76, No.7, pp.1898-99, 1993.

    (c) B.R. LAWN, L.M. BRAUN, S.J. BENNISON and R.F. COOK, Reply to «Comment on "Role of grain size in the strength and *R*-curve properties of alumina"», *J. Am. Ceram. Soc.*, Vol.76, No.7, pp.1900-901, 1993.

25. A.V. VIRKAR, D.K. SHETTY and A.G. EVANS, Grain-size dependence of strength, *J. Am. Ceram. Soc.*, Vol.64, No.3, pp.56-57, 1981.

26. T. FETT, D. MUNZ, J. SEIDEL, M. STECH and J. RÖDEL, Correlation between long and short crack *R*-curves in alumina using the crack opening displacement and fracture mechanical weight function approach, *J. Am. Ceram. Soc.*, Vol.79, No.5, pp.1189-96, 1996.

27. R.W. STEINBRECH, A. REICHL and W. SCHAARWÄCHTER, *R*-curve behaviour of long cracks in alumina, *J. Am. Ceram. Soc.*, Vol.73, No.7, pp.2009-15, 1990.

28. J. RÖDEL, J.F. KELLY and B.R. LAWN, In situ measurements of bridged crack interfaces in the scanning electron microscope, *J. Am. Ceram. Soc.*, Vol.73, No.11, pp.3313-18, 1990.

29. J. SEIDEL and J. RÖDEL, Measurement of crack tip toughness in alumina as a function of grain size, *J. Am. Ceram. Soc.*, Vol.80, No.2, pp.433-38, 1997.

30. J.C. HAY and K.W. WHITE, Grain-bridging mechanisms in monolithic alumina and spinel, *J. Am. Ceram. Soc.*, Vol.76, No.7, pp.1849-54, 1993.

31. J.J. Swab and G.D. Quinn, *Fractography of Advanced Structural Ceramics: Results from the VAMAS Round Robin Exercise*, VAMAS, Technical Working Area 3, Report No.19, ISSN 1016-2186, 1995.

32. A.G. EVANS, D.R. BISWAS and R.M. FULRATH, Some effects of cavities on the fracture of ceramics, II: Spherical cavities, *J. Am. Ceram. Soc.*, Vol.62, No.1-2, pp.101-06, 1979.

33. F.I. BARATTA, Stress intensity factor estimates for a peripherally cracked spherical void and a hemispherical surface pit, *J. Am. Ceram. Soc.*, Vol.61, pp.490-93, 1978.

34. F.I. BARATTA, Refinement of stress intensity factor estimates for a peripherally cracked spherical void and a hemispherical surface pit, *J. Am. Ceram. Soc.*, Vol.64, No.3-4, 1981.

35. D.J. GREEN, Stress intensity factor estimates for annular cracks at spherical voids, *J. Am. Ceram. Soc.*, Vol.63, pp.342-44, 1980.

36. T. FETT, Stress intensity factors and weight function for a void with an annular crack, *Int. J. of Fract.*, Vol.67, R41-R47, 1994.

37. (a) R.A. EUBANKS, Stress concentration due to a hemispherical pit at a free surface, *J. Appl. Mech.*, Vol.21, pp.57-62, 1954.

(b) G.-Q. ZHU, J. E. RITTER, K. JAKUS and S. BHATTACHARYA, Stress intensity factor for a peripherally cracked spherical cap, *J. Am. Ceram. Soc.*, Vol.80, pp.2445-48, 1997.

38. H. BÖCKNER, A novel principle for the computation of stress intensity factors, *Z. Angew. Math. Phys.*, Vol.50, pp.529-46, 1970.

39. H. TADA, P. C. PARIS and G. R. IRWIN, *The Stress Analysis Handbook*, Paris Productions, St. Louis 1985.

40. T. FETT, An estimation of local stress intensity factors for semi-elliptical surface cracks, *Eng. Fract. Mech.*, Vol.34, pp.883-90, 1989.

41. J.C. NEWMAN and I.S. RAJU, An empirical stress intensity factor equation for the surface crack, *Eng. Fract. Mech.*, Vol.15, pp.185-92, 1981.

42. T.A. CRUSE and P.M. BESUNER, Residual life prediction for surface cracks in complex structural details, *J. of Aircraft*, Vol.12, pp.369-75, 1975.

43. B.D. FLINN, R.K. BORDIA and J. RÖDEL, Evolution of strength determining flaws during sintering, pp.13-20, in: R.M. German, G.L. Messing and R.G. Cornwall [eds.], *Sintering Technology*, Marcel Dekker, New York 1996.

44. E.B. SLAMOWICH and F.F. LANGE, Densification of large pores, I: Experiments, *J. Am. Ceram. Soc.*, Vol.75, No.9, pp.2498-508, 1992.

45. E.B. SLAMOWICH and F.F. LANGE, Densification of large pores, II: Driving potentials and kinetics, *J. Am. Ceram. Soc.*, Vol.76, No.6, pp.1584-90, 1993.

46. S.J. BENNISON and M.P. HARMER, Swelling of Hot-Pressed Al_2O_3, *J. Am. Ceram. Soc.*, Vol.68, No.11, pp.591-597, 1985.

47. M. HOFFMAN, P. MERKERT, A. ZIMMERMANN, J. RÖDEL, M. KNECHTEL, F. MESCHKE and M. STERNITZKE, *Crack Initiation Processes in Alumina Based Ceramics*, presented at PacRim2, Cairns, Australia, 1996.

48. Q. MA and D. CLARKE, Piezospectroscopic determination of residual stresses in polycrystalline alumina, *J. Am. Ceram. Soc.*, Vol.77, No.2, pp.298-302, 1994.

49. P. MERKERT, M. HOFFMAN and J. RÖDEL, Detection of prefracture microcracking in Al_2O_3 by acoustic emission, *J. Eur. Ceram. Soc.* [in press].

50. T. IKEGAMI and Y. MORIYOSHI, Evaluation of grain-growth parameters, *J. Am. Ceram. Soc.*, Vol.68, No.11, pp.597-603, 1985.

51. R.L. COBLE and W.D. KINGERY, Effect of porosity on physical properties of sintered alumina, *J. Am. Ceram. Soc.*, Vol.39, No.11, pp.377-385, 1956.

52. R.M. SPRIGGS, Expression for effect of porosity on elastic modulus of polycrystalline refractory materials, particularly aluminum oxide, *J. Am. Ceram. Soc.*, Vol.44, No.12, pp.628-629, 1961.

53. K.K. PHANI and S.K. NIYOGI, Young's modulus of porous brittle solids, *J. Mater. Sci.*, Vol.22, pp.257-263, 1987.

54. S.K. DUTTA, A.K. MUKHOPADHYAY and D. CHAKRABORTY, Assessment of strength by Young's modulus and porosity: a critical evaluation, *J. Am. Ceram. Soc.*, Vol.71, No.11, pp.942-947, 1988.

55. A.S. WAGH, J.P. SINGH and R.B. POEPPEL, Dependence of ceramic fracture properties on porosity, *J. Mater. Sci.*, Vol.28, pp.3589-93, 1993.

56. N. RAMAKRISHNAN and V.S. ARUNACHALAM, Effective elastic moduli of porous ceramic materials, *J. Am. Ceram. Soc.*, Vol.76, No.11, pp.2745-2752, 1993.

57. D.J. GREEN, C. NADER and R. BREZNY, The elastic behaviour of partially-sintered alumina, in: J.E. Blendell, C.A. Handwerker and W.A. Kaysser [eds.], *Ceramic Transactions*, Vol.7, pp.345-356, Am. Cer. Soc., Westerville, OH, 1990.

58. D. HARDY and D.J. GREEN, Mechanical properties of a partially sintered alumina, *J. Eur. Ceram. Soc.*, Vol.15, pp.769-775, 1995.

59. E. RYSHKEWITCH, Compression strength of porous sintered alumina and zirconia, *J. Am. Ceram. Soc.*, Vol.36, No.2, pp.65-68, 1953.

60. W. DUCKWORTH, Discussion of Ryshkewitch paper, *J. Am. Ceram. Soc.*, Vol.36, No.2, p.68, (1953).

61. P. QUIRMBACH, M. WOLF, R.J. BROOK and H.-W. HENNECKE, Development of microstructure during pressureless sintering of alumina, *J. Eur. Ceram. Soc.*, Vol.10, 1992. 51-57.

62. D.C.C. LAM, F.F. LANGE and A.G. EVANS, Mechanical properties of partially dense alumina produced from powder compacts, *J. Am. Ceram. Soc.*, Vol.77, No.8, pp.2113-2117 (1994).

63. T. OSTROWSKI, A. ZIEGLER, R.K. BORDIA and J. RÖDEL, Evolution of Young's modulus, strength and microstructure during liquid phase sintering, *J. Am. Ceram. Soc.*, Vol.81, No.7, pp.1852-60, 1997.

64. B.D. FLINN, R.K. BORDIA, A. ZIMMERMANN and J. RÖDEL, Evolution of defect size and strength of porous alumina during sintering, *J. Am. Ceram. Soc.* [in press].

65. R.L. COBLE, Diffusion models for hot pressing with surface energy and pressure effects as driving forces, *J. Am. Ceram. Soc.*, 41, No.12, pp.4798-4807, 1970.

66. W.D. KINGERY and B. FRANCOIS, Sintering of cristalline oxides, I: Interaction between grain boundaries and pores, in: G.C. KUCZYNSKI, N.A. HOOTON and G.F. GIBBON, *Sintering and Related Phenomena*, pp.471-98 Gordon Breach, New York 1967.

67. B.J. KELLETT and F.F. LANGE, Experiments on pore closure during hot isostatic pressing and forging, *J. Am. Ceram. Soc.*, Vol.71, No.1, pp.7-12, 1988.

68. H. SCHUBERT AND W.A. KAYSSER, Hiping of alumina, in: J.E. Blendell, C.A.Handwerker and W.A. Kaysser, *Ceramic Transactions*, Vol.7, pp.506-526, Am. Cer. Soc., Westerville, OH, 1990.

69. D.-W. SHIN, K.K. ORR and H. SCHUBERT, Microstructure-mechanical property relationships in hot-isostatically pressed alumina and zirconia-toughened alumina, *J. Am. Ceram. Soc.*, Vol.73, No.5, pp.1181-1188, 1990.

70. K.-S. OH, D.-Y. KIM and S.-J. CHO, Shrinkage of large isolated pores during hot isostatic pressing of presintered alumina ceramics, *J. Am. Ceram. Soc.*, Vol.78, No.9, pp.2537-40, 1995.

71. G. PETZOW and H.E. EXNER, Particle rearrangement in solid state sintering, *Z. Metallk.*, Vol.67, No.9, pp.611-618, 1976.

72. L.T. KUHN, R.M. MCMEEKING and F.F. LANGE, A model for powder consolidation, *J. Am. Ceram. Soc.*, Vol.74, No.3, pp.682-685, 1991.

73. P. BROSS and H.E. EXNER, Computer simulation of sintering processes, *Acta Metall.*, Vol.27, pp.1013-1020, 1979.

74. W. ZHANG and J. H. SCHNEIBEL, The sintering of two particles by surface and grain boundary diffusion – a two-dimensional numerical study, *Acta Metall. Mater.*, Vol.43, No.12, pp.4377-4386, 1995.

75. J. SVOBODA and H. RIEDEL, Quasi-equilibrium sintering for coupled grain boundary and surface diffusion, *Acta Metall. Mater.*, Vol. 43, No.2, pp.499-506, 1995.

76. J. SVOBODA, H. RIEDEL and H. ZIPSE, Equilibrium pore surfaces, sintering stresses and constitutive equations for the intermediate stage and late stage of sintering, I: Computation of equilibrium surfaces, *Acta Metall. Mater.*, Vol.42, No.2, pp.435-443, 1994.

77. H. RIEDEL, V. KOZAK and J. SVOBODA, Densification and creep in the final stage of sintering, *Acta Metall. Mater.*, Vol.42, No.9, pp.3093-3103, 1994.

78. T. FETT, D. MUNZ, J. SEIDEL, M. STECH and J. RÖDEL, Correlation between long and short crack R-curves in alumina using the crack opening displacement and fracture mechanical weight function approach, *J. Am. Ceram. Soc.*, Vol.79, No.5, pp.1189-1196, 1996.

79. T. OSTROWSKI, *Mechanische Eigenschaften poröser Keramiken*, Ph. D. Thesis, TU Darmstadt, 1997.

80. Y.-W. MAI and B. R. LAWN, Crack-interface grain bridging as a fracture resistance mechanism in ceramics, II: Theoretical fracture mechanics model, *J. Am. Ceram. Soc.*, Vol.70, No.4, pp.289-94, 1987.

81. S. BENNISON and B. LAWN, Role of interfacial grain-bridging sliding friction in the crack-resistance and strength properties of nontransforming ceramics, *Acta Metall.*, Vol.37, No.10, pp.2659-71, 1989.

82. R. STEINBRECH, A. REICHL and W. SCHAARWÄCHTER, R-curve behaviour of long cracks in alumina, *J. Am. Ceram. Soc.*, Vol.73, No.7, pp.2009-15, 1990.

83. J. RÖDEL, J.F. KELLY and B.R. LAWN, In situ measurements of bridged crack interfaces in the scanning electron microscope, *J. Am. Ceram. Soc.*, Vol.73, No.11, pp.3313-18, 1990.

84. M.P. HARMER, H.M. CHAN and G.A. MILLER, Unique opportunities for microstructural engineering with duplex and laminar ceramic composites, *J. Am. Ceram. Soc.*, Vol.75, No.7, pp.1715-28, 1992.

85. R. LAKSHMINARAYANAN, D. SHETTY and R. CUTLER, Toughening of layered ceramic composites with residual surface compression, *J. Am. Ceram. Soc.*, Vol.79, No.1, pp.79-87, 1996.

86. D. MARSHALL, J. RATTO and F. LANGE, Enhanced fracture toughness in layered microcomposites of Ce-ZrO_2 and Al_2O_3, *J. Am. Ceram. Soc.*, Vol.74, No.12, pp.2979-87, 1991.

87. M.P. RAO, A.J. SÁNCHES-HERENCIA, G.E. BELTZ, R.M. MCMEEKING and F.F. LANGE, Laminar ceramics that exhibit a threshold strength, *Science*, Vol.286, pp.102-105, 1999.

88. R. MOON, K. BOWMAN, K. TRUMBLE and J. RÖDEL, Fracture resistance curve behaviour of multilayered alumina-zirconia composites produced by centrifugation, *Acta Mater.*, Vol.49, pp.995-1003, 2001.

89. R. MOON, M. HOFFMAN, J. HILDEN, K. BOWMAN, K. TRUMBLE and J. RÖDEL, A Weight function analysis on the R-curve behaviour of multilayered alumina-zirconia composites, *J. Am. Ceram. Soc.* [in press], October 2000.

90. A.J. BLATTNER, R. LAKSHMINARAYANAN and D.K SHETTY, Toughening of layered ceramic composites with residual surface compression: effects of layer thickness, *Eng. Frac. Mech.*, Vol.68: pp.1-7, 2001.

91. J.C. CHANG, B.V. VELAMAKANNI, F.F. LANGE and D.S. PEARSON, Centrifugal Consolidation of Al_2O_3 and Al_2O_3/ZrO_2 Composite Slurries Vs Interparticle Potentials: Particle Packing and Mass Segregation. *J. Am. Ceram. Soc.*, 1991, 74, No.9, pp.2201-204.

92. W. HUISMAN, T. GRAULE and L. J. GAUCKLER, Alumina of High Reliability by Centrifugal Casting. J. Euro. Ceram. Soc. 1995, 15: 811-21.

93. Z.-H. JIN AND R.C. BATRA, R-curve and Strength Behaviour of a Functionally Graded Material. Mater. Sci. and Eng., 1998, A242: 70-76.

94. T.-J. CHUNG, A. NEUBRAND, J. RÖDEL and T. FETT, Fracture Toughness and R-Curve Behaviour of Al_2O_3/Al FGMs, to be published in Proceedings of FGM2000, Estes Park, CO, USA 2000

95. T. FETT, D. MUNZ and Y.Y. YANG, Direct Adjustment Procedure for Weight Function Analysis of Graded materials. Fat. Fract. Engng Mater. Struct., 2000, 23: 191-198.

96. R. MOON, M. HOFFMAN, J. HILDEN, K. BOWMAN, K. TRUMBLE and J. RÖDEL, A weight function analysis of *R*-curve behaviour in gradient alumina-zirconia composites, [in:] *Proceedings of 6th Functionally Graded Materials conference* [in press], (citations of 15 and 17 should be consistent).

97. J. CHANG, F. LANGE and D. PEARSON, Pressure sensitivity for particle packing of aqueous Al_2O_3 slurries vs. interparticle potential, *J. Am. Ceram. Soc.*, Vol.77, No.5, pp.1357-60, 1994.

98. O. SBAIZERO and E. LUCCHINI, Influence of Residual Stresses on the Mechanical Properties of a Layered Ceramic Composite, *J. Euro. Ceram. Soc.*, Vol.16, pp.813-18, 1996.

99. B.V. VELAMAKANNI, J.C. CHANG, F.F. LANGE and D.S. PEARSON, New method for efficient colloidal particle packing via modulation of repulsive lubrication hydration forces, *Langmuir*, Vol.6, No.7, pp.1323-25, 1990.

100. R. MOON, K. BOWMAN, K. TRUMBLE and J. RÖDEL, A comparison of *R*-curves from SEVNB and SCF fracture toughness test methods on multilayered alumina-zirconia composites, *J. Am. Ceram. Soc.*, Vol.83, No.2, pp.445-47, 2000.

101. J. KÜBLER, Fracture toughness using the SEVNB method: preliminary results, *Ceram. Eng. & Sci. Proc.*, Vol.18, No.4, pp.155-162, 1997.

102. M. STECH and J. RÖDEL, Method for measuring short-crack *R*-curves without calibration parameters: case studies on alumina and alumina/aluminum composites. *J. Am. Ceram. Soc.*, Vol.79, No.2, pp.291-97, 1996.

103. R.J. MOON, Static Fracture Behaviour of Multilayer Alumina-Zirconia Composites, PhD Thesis, Purdue University, May 2000.

104. H.F. BUECKNER, A novel principle for the computation of stress intensity factors, *Z. Angew Math. Mech.*, Vol.50, pp.529-46, 1970.

105. T. FETT and D. MUNZ, Influence of crack-surface interactions on stress intensity factor in ceramics, *J. Mater. Sci. Lett.*, Vol.9, pp.1403-406, 1990.

106. T. FETT and D. MUNZ, Determination of fracture toughness at high temperature after subcritical crack extension, *J. Am. Ceram. Soc.*, Vol.75, No.11, pp.3133-36, 1992.

107. T. FETT, Determination of residual stresses in components using the fracture mechanics weight function, *Engineering Fracture Mechanics*, Vol.55, No.4, pp.571-76, 1996.

108. J.D. FRENCH, J. ZHAO, M.P. HARMER, H.M. CHAN and G.A. MILLER, Creep of duplex microstructures, *J. Am. Ceram. Soc.*, Vol.77, No.11, pp.2857-65, 1994.

109. P.Z. CAI, D.J. GREEN and G.L. MESSING, Constrained densification of alumina/zirconia hybrid laminates, II: Viscoelastic stress computation, *J. Am. Ceram. Soc.*, Vol.80, No.8, pp.1940-48, 1997.

110. C.J. GILBERT and R.O. RITCHIE, On the quantification of bridging tractions during subcritical crack growth under monotonic and cyclic fatigue loading in a grain-bridging silicon carbide ceramic, *Acta Metall.*, Vol.46, No.2, pp.609-16, 1998.

111. K.-S. SOHN, S. LEE and S. BAIK, Analytical modeling for bridging stress function involving grain size distribution in a polycrystalline alumina, *J. Am. Ceram. Soc.*, Vol.78, No.5, pp.1401-405, 1995.

112. J.C. HAY and K.W. WHITE, Grain-bridging mechanisms in monolithic alumina and spinel, *J. Am. Ceram. Soc.*, Vol.76, No.7, pp.1849-54, 1993.

113. J.E. SRAWLEY and B. GROSS, Side-cracked plates subject to combined direct and bending forces. Cracks and fracture, *ASTM STP*, Vol.601, pp.559-79, 1976.

114. F. ERDOGAN, Fracture mechanics of functionally graded materials, *Composites Engineering*, Vol.5, No.7, pp.753-70, 1995.

115. Z.-H. JIN and R.C. BATRA, Some basic fracture mechanics concepts in functionally graded materials, *J. Mech Phys Solids.*, Vol.44, No.8, pp.1221-35, 1996.

116. C. HILLMAN, Z. SUO and F.F. LANGE, Cracking of laminates subjected to biaxial tensile stresses, *J. Am. Ceram. Soc.*, Vol.79, No.8, pp.2127-33, 1996.

117. R.G. MUNRO, Evaluated material properties for a sintered α-alumina, *J. Am. Ceram. Soc*, Vol.80, No.8, pp.1919-28, 1997.